Structure, photoluminescence emissions, and photocatalytic activity of Ag_2SeO_3: a joint experimental and theoretical investigation

Ivo M. Pinatti [a*], Aline B. Trench [b], Ana C. M. Tello [b], Paula F. S. Pereira [b], Josiane C. Souza [b], Marcio D. Teodoro [c], Ieda L. V. Rosa [b], Juan Andrés [d], Elson Longo [b], and Alexandre Z. Simões [a]

[a] *Faculty of Engineering of Guaratinguetá, São Paulo State University (UNESP), 12516-410, Guaratinguetá, SP, Brazil.*
[b] *CDMF, LIEC, Federal University of São Carlos (UFSCar), P.O. Box 676, São Carlos 13565-905, Brazil.*
[c] *Physics Department, Federal University of São Carlos (UFSCar), P.O. Box 676, São Carlos 13565-905, Brazil.*
[d] *Department of Analytical and Physical Chemistry, University Jaume I (UJI), Castelló 12071, Spain.*
**corresponding author: ivopinatti@hotmail.com*

Abstract

In this paper, we relate the synthesis of silver selenite (Ag_2SeO_3) by different methods [sonochemistry, ultrasonic probe, coprecipitation, and microwave-assisted hydrothermal]. These microcrystals presented structural long-range order as confirmed by X-ray diffraction (XRD) and Rietveld refinements, and structural short-range order as confirmed by Fourier transform infrared (FT-IR), and Raman spectroscopies. X-ray photoelectron spectroscopy (XPS) provided information about the surface of the samples indicating that they were pure. The microcrystals presented different shape and size due to synthesis method as observed by field emission scanning electron microscopy (FE-SEM). The optical properties of these microcrystals were evaluated by ultraviolet−visible (UV−vis) spectroscopy and photoluminescence (PL) measurements. Thermal analysis confirmed the temperature stability of the as-synthetized samples. Further trapping experiments prove that the holes and hydroxyl radical, in minor extent, are responsible for the photocatalytic reactions. To complement and rationalize the experimental results, first-principles calculations have been performed within the framework of density functional theory. The experimental results are sustained by DFT calculations that decipher the geometric, energetic, and structural parameters as well as vibrational frequencies; further, the electronic properties (band structure diagram and density of states) of the bulk and corresponding surfaces of Ag_2SeO_3 were also investigated. On the basis of the calculated values of the surface energies, a map of the available morphologies was obtained by using Wulff construction and compared to the experimental FE-SEM images. By determining the energy profiles associated with the transformation process between different morphologies obtained along the synthesis method, we are capable to find a correlation between morphology and photocatalytic activity, along with photodegradation of Rhodamine B dye under UV light, based on the different numbers

of unsaturated superficial Ag and Se cations (local coordination, i.e., clusters) of each surface.

Keywords: silver selenite; photoluminescence; photocatalysis; DFT calculations.

Introduction

In recent decades, metallic selenites have attracted great attention because of their different chemical structures and advanced physical properties such as pyroelectricity, ferroelectricity and piezoelectricity, and their important role in the human health specially because selenium is an elemental component of several selenoproteins [1]. Selenites can be considered important lone-pair oxyanions, in which the presence of stereoactive nonbonded electron pairs are presented [2] and active free electron pair of the Se^{4+} cations can induce second-order Jahn-Teller distortions and the formation of non-centrosymmetric or polar structures. [2–5]

Some examples of metallic selenite include $Pb(SeO_3)_2$ and two modifications of $Sn(SeO_3)_2$ (α- and β-) which were synthesized at low-hydrothermal conditions [6]. Crystal structures of $SrSeO_3$ and $CaSeO_3$ and their respective relationships with molybdomenite- and monazite-type compounds were also prepared by hydrothermal methodology [7]. $AGa_3F_6(SeO_3)_2$ (A = Rb, Cs) [8] materials were also studied. Hydrothermal synthesis of $Mn(SeO_3)_2$ [9], and orthorhombic phase of β-$ZnSeO_3$ [10] which was prepared by treating ZnO with selenous acid solutions were easily obtained. Moreover, orthorhombic isomorphs crystal chemistry of many transition metals of $MSeO_3$ and $MTeO_3$ (M = Mg, Mn, Co, Ni, Cu, and Zn) obtained under high pressure and temperature were considered [11], as well as bismuth [5,12–14] and indium selenite [15]. Other compounds containing selenium and rare earth elements of different structure type were studied in terms of its solubility, magnetic susceptibility among other properties [16–21].

Silver-contained materials can be considered outstanding compounds for biomedical application because of its low toxicity and bacteriostatic properties, and they can also be used as biomarker and other medical applications. These materials have already been studied as candidates for antibacterial agents, besides their SPR effect. [22–24] Our research group has demonstrated in other works the successful synthesis, characterization, as well as photocatalytic, photoluminescent and bactericidal applications of silver-based materials such as Ag_2WO_4 [25–32], Ag_2MoO_4 [33,34], Ag_2CrO_4 [35–

[38], $AgVO_3$ [39–42], $Ag_4V_2O_7$ [43,44], and Ag_3PO_4 [45–47]. All of these materials present different morphologies due to synthesis methods used which in turn are responsible for different applications. Moreover, high efficient photocatalytic activity of these materials due to different methods [48,49] or use of surfactant [50,51] were recently obtained.

Based on the above considerations, the coupling of Ag and Se in a single building block could give rise to functional activity over others metallic selenites. However, to our best knowledge, there is no work related to the structure, photoluminescence (PL) emissions, and photocatalytic activity of silver selenite Ag_2SeO_3. Accordingly, in this paper, we report the synthesis of Ag_2SeO_3 by sonochemistry (SC), ultrasonic probe (UP) coprecipitation (CP), and microwave assisted hydrothermal (MH) methods. These microcrystals were structurally characterized, and first-principles calculations within the framework of density functional theory (DFT) were employed to obtain atomic-level information on the geometry and electronic structure, local bonding, band structure, and density of states (DOS). In addition, the experimental and theoretical structure, vibrational frequency and morphology are compared to rationalize the PL emissions and photocatalytic activity, for first time.

Experimental Section

Synthesis

Ag_2SeO_3 was synthesized by the SC, UP, CP, and MH methods. Silver nitrate ($AgNO_3$), and selenium oxide (SeO_2) were purchased from Sigma-Aldrich. In a typical procedure, stoichiometric amounts of Ag^+ and SeO_3^{2-} solutions were prepared and mixed to form a suspension. In the SC methodology, the suspension was ultrasonicated for 1h at room temperature in a Branson (model 1510) ultrasonic cleaner, and the crystals were collected after turning off the ultrasonic equipment. In the UP methodology, an ultrasonic probe sonicator (Sonics, GEX 750) was used with the probe inserted into the suspension and maintained for 1 hour at room temperature. Along the CP method, the suspension was maintained under stirring at 90 °C for 1h and the precipitated was collected after turning off the stirring. In the MH method, the suspension was transferred to the MH system and maintained at 140 °C for 1h. After that, all the samples were naturally cooled to room temperature, the precipitates were separated by centrifugation, washed with deionized water to remove any remaining ions. Finally, the crystals were collected and then dried in an oven at 60 °C for 12 h.

Characterization

Thermal behavior was studied with a STA (TG/DTA) 409 Netzsch instrument. Samples weight were about 24.5 mg and heating rate was 3 °C/min. The measurement was carried out in O_2 (50 mL/min) atmosphere. The materials were structurally characterized by X-ray diffraction (XRD) using a D/Max-2000PC Rigaku (Japan) diffractometer with Cu Kα radiation (λ = 1.5406 Å) in the 2θ range from 10° to 60° in the normal routine with a scanning velocity of 2°/min and from 5° to 110° with a scanning velocity of 0.2°/min in the Rietveld routine. X-ray photoelectron spectroscopy (XPS) was performed using a ScientaOmicron ESCA+ spectrometer with a high-performance hemispheric analyzer (EA 125) with monochromatic Al Kα (hν = 1486.6 eV) radiation as the excitation source. The operating pressure in the ultrahigh vacuum chamber (UHV) during analysis was $2x10^{-9}$ mbar. Energy steps of 50 and 20 eV were used for the survey and high resolution spectra measurements, respectively. All data analysis was performed using CASA XPS Software (Casa Software Ltd, UK). Micro-Raman spectroscopy was conducted on a Horiba Jobin-Yvon (Japan) spectrometer charge-coupled device detector and argon-ion laser (Melles Griot, United States) operating at 633 nm with a maximum power of 17 mW. Fourier transform infrared (FTIR) spectroscopy was performed at room temperature using a Jasco FT/IR-6200 (Japan) spectrophotometer operated in diffuse reflectance mode (DRIFT). The spectra have a resolution of 4 cm^{-1} and 32 accumulations per measurement in the range of 400−4000 cm^{-1}. These measurements were performed on powder mix which was composed of 1% by weight of each sample mixed with 99% by weight of KBr (99%, Sigma-Aldrich). UV-vis diffuse reflectance spectroscopy (UV-vis DRS) were taken using a spectrophotometer (Varian, model Cary 5G) in a diffuse-reflectance mode. The shapes and sizes of these microcrystals were observed with a field emission scanning electron microscope (FE-SEM) model Inspect F50 (FEI Company, Hillsboro, OR) operated at 5 kV. Photoluminescence (PL) measurements were performed at room temperature with the samples excited by a 355 nm laser (Cobolt/Zouk) focused on a 20 um spot, 50 μW of power. The backscattered luminescence was dispersed by a 20 cm spectrometer with the signal detected by a charged coupled device detector (Andor technologies).

Theoretical methods and model systems

First principle calculations were carried out using the CRYSTAL17 computational package [52]. The crystal structure of Ag_2SeO_3 was studied by means of DFT calculations at the hybrid exchange-correlation functional level, developed by Lee, Yang and Parr (B3LYP) [53]. It was used extended Gaussian basis sets type 86- pob_TZVP [54] for the Se and O atoms, while the core pseudo-potential SC-doll_1998 [55] was chosen for Ag. The accuracy of the Coulomb and exchange integral calculations (TOLINTEG) was controlled by five parameters set to 10^{-8}, 10^{-8}, 10^{-8}, 10^{-8}, and 10^{-16}, which provide high numerical accuracy. In addition, to provide a more accurate description of the structure crystalline the Mohnkhost-Pack [56] network was defined as 8, featuring eight k-points to describe the region of high symmetry of the crystalline structure. The electronic band structure, DOS and partial DOS projected on atoms and orbitals of Ag_2SeO_3 were calculated along the appropriate high-symmetry directions of the corresponding irreducible Brillouin zone.

The equilibrium morphology of the crystal of Ag_2SeO_3 monoclinic (*P21/c*) was calculated based on the classic Wulff construction [57], by minimizing the total surface energy (E_{surf}) at a fixed volume, providing a simple relationship between the E_{surf} of the plane (hkl) and its distance in the normal direction from the center of the crystallite [58]. Eight surfaces with index: (011), (100), (001), (021), (111), (110), (010) and (101) were used to model the ideal morphology and by tuning of the $E_{surf}^{(hkl)}$ were the complete map of available morphologies is obtained, which were compared with the experimental morphologies obtained from FE-SEM images. E_{surf} is calculated according to equation:

$$E_{surf}^{(hkl)} = \frac{E_{slab} - nE_{bulk}}{2A} \qquad \text{Eq. 1}$$

where E_{slab} is the total energy per repeating cell of the slab, E_{bulk} is the total energy of the perfect crystal per molecular unit, n is the number of bulk units, and A is the surface area per repeating cell of the two sides of the slab. The electronic properties of the surfaces studied, are also are reported. In order to analyze the relation between E_{surf} and the geometric characteristics of the exposed surfaces, the dangling bond density (D_b) was calculated from the number of broken bonds created per unit cell (N_b) on a particular surface of area *A*, according to the expression: [59]

$$D_b = \frac{N_b}{A} \qquad \text{Eq. 2}$$

To rationalize the pathways connecting the different morphologies shapes predicted, the polyhedron energy (E_{poly}) was calculated by summing the contributions of each facet to the morphological shape and the corresponding E_{surf} values, according to the expression:

$$E_{poly} = \sum c_{(hkl)} E_{surf}^{(hkl)} \qquad \text{Eq. 3}$$

where $c_{(hkl)}$ is the percent contribution of the surface area to the total surface area of the polyhedron, and $E_{surf}^{(hkl)}$ is the surface energy of the corresponding surface.

Photocatalysis

The photoactivity of the samples obtained was investigated for the degradation of Rhodamine B (RhB) under ultraviolet (UV) irradiation using 6 lamps (Philips TUV, 15 W). 50 mg of each catalyst were used, which were added to a beaker containing 50 mL of RhB (1.0 x 10^{-5} mol / L). The suspension was placed in an ultrasonic bath (Branson, model 1510; frequency 42 kHz) for 10 minutes and then stirred in the dark for 30 minutes for the absorption-adsorption equilibrium process. The suspension was then exposed to UV light, under constant stirring and maintaining the temperature at 20 °C and at certain times, aliquots were removed, which were centrifuged and the supernatant were monitored through the maximum absorption wavelength of RhB (λ_{max} = 554 nm) using a UV-vis spectrophotometer (V-660, JASCO).

Results and Discussion

Thermal analysis

TG/DTA measurements were carried out to determine the decomposition temperatures and phase transformations of the Ag_2SeO_3 samples. The curves are presented in Fig. 1. The results may suggest the following thermal processes which occur under the experimental conditions in O_2 atmosphere [60]:

$$Ag_2SeO_{3\,(s)} \rightarrow Ag_2SeO_{3\,(l)} \quad (1)$$

$$Ag_2SeO_{3\,(l)} \rightarrow 2Ag_{(s)} + SeO_2 + 1/2\,O_{2\,(g)} \quad (2)$$

$$2Ag_{(s)} \rightarrow 2Ag_{(l)} \quad (3)$$

Through the DTA curve, at 535 ºC, there was an endothermic process related to the melt of Ag_2SeO_3, showed by the reaction (1). Reaction (2) represents the decomposition of the Ag_2SeO_3 between 560 ºC to 930 ºC with a ≈ 40% reduction in sample mass, corroborating the two exothermic processes between 640 ºC and 730 ºC, determined in the DTA curve , except for the Ag_2SeO_3-UP sample that in this region presented an endothermic process. The endothermic peak at 946 ºC was attributed to the melt of the metallic Ag, as shown by reaction (3) [60,61]. In a nitrogen atmosphere, reaction (2) takes place at a slightly lower temperature (the difference in DTG maxima is ca. 10 °C) than in air, thus corroborating the oxygen evolution [3,60,62]. TG curves of the samples at a temperature close to 1000 ºC, show no stabilization of any silver oxide, which corroborated with the thermodynamic studies at high O_2 pressures between 1 to 100 atm by Assal et al. [63].

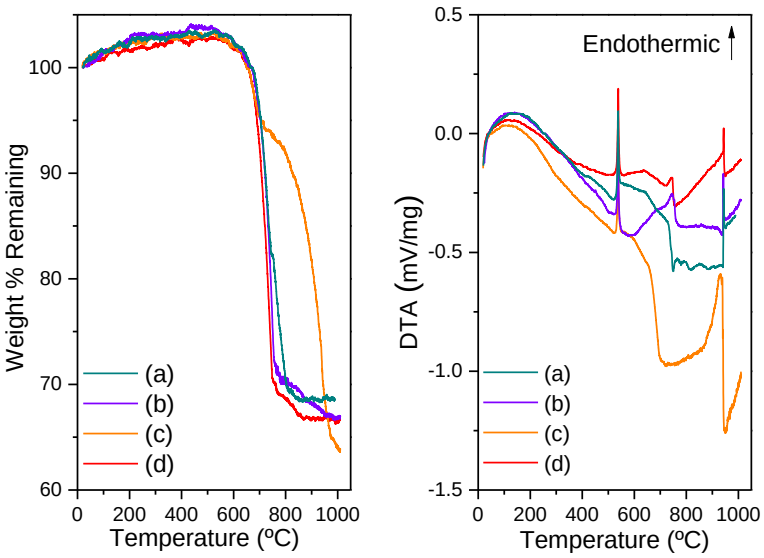

Fig. 1. Simultaneous TG and DTA curves for the thermal decomposition of the samples in O_2 using a heating rate of 3 °C.min^{-1}. (a) Ag_2SeO_3-SC, (b) Ag_2SeO_3-UP, (c) Ag_2SeO_3-CP, and (d) Ag_2SeO_3-MH.

XRD

Fig. 2 shows the XRD patterns of the Ag_2SeO_3 samples. It was observed well defined and intense peaks related to the monoclinic phase and space group *P2₁/c* (Z = 4) which agrees with the inorganic crystal structure database (ICSD) card no 78-388. These results confirm that all samples are monophasic and without secondary phases, indicating they are crystalline and present structural long-range order [60].

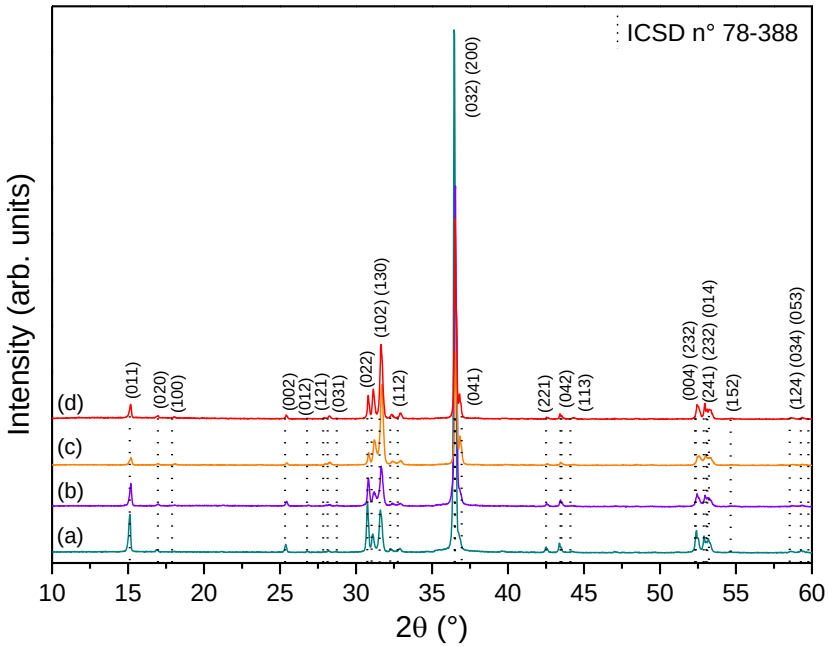

Fig. 2. XRD patterns of the (a) Ag_2SeO_3-SC, (b) Ag_2SeO_3-UP, (c) Ag_2SeO_3-CP, and (d) Ag_2SeO_3-MH samples.

Structural properties of the Ag_2SeO_3 samples were performed by Rietveld refinement method. The refined parameters include preferred orientation, lattice parameters and shift lattice constants, atomic functional positions among others instrumental and sample parameters. The background was adjusted by a Chebyshev function and the peak profile by a convolution of Thompson-Cox-Hastings pseudo-Voigt (pV-TCH) function. The asymmetry function and the anisotropy in the half-width of the reflections was considered according to Finger et al. [64] and Stephens [65], respectively. The experimental lattice parameters, unit cell volume, statistical parameters of quality (χ^2 and R_{Bragg}), and the atomic positions of Ag_2SeO_3 microcrystals in different synthesis methods were evaluated using the general structure analysis system (GSAS) software [66].

Fig. SI-1 (a–d) shows the Rietveld refinement graphic of Ag_2SeO_3 microcrystal obtained by different synthesis methods. It can be observed that all data present a good fit between the calculated and observed XRD patterns, which is confirmed through the

goodness of fit (χ^2) and *R*-value (R_{Bragg}), presenting satisfactory values for a quality refinement (see Table 1). Table 1 shows the experimental obtained and theoretical calculated data from Rietveld refinement method, such as lattice parameters, cell volume and the statistical parameters (χ^2 and R_{Bragg}). It is possible to confirm by the Rietveld refinement method the absence of additional phase in Ag_2SeO_3 microcrystal obtained by SC, UP, CP and MH methods, showing that the Rietveld refinement method was performed effectively, corroborating with XRD patterns and ICSD Nº 78-388 card [60], which belongs a monoclinic phase and space group $P2_1/c$ (Z = 4).

No significant changes were observed among the samples, attesting the structural long-range order of all samples. Table SI-1 presents the atomic coordinates (x, y, z) for Ag, Se and O atoms obtained by Rietveld refinements and Table SI-2 shows the crystallographic data of Rietveld refinement. It is possible to note a local distortion in the atomic positions (x, y, z) of the atoms, being more prominent in the O positions. Finally, all synthesis methods were efficient to obtain the phase, without amorphous phase. Moreover, all methods enhance the organization of the [SeO_3] and [AgO_6] clusters within the crystal lattice, preventing the formation of structural defects (stresses and strains), as observed by the higher crystallinity of all the samples.

Table 1. Lattice parameters, unit cell volume and statistical parameters of quality obtained through Rietveld refinements of Ag_2SeO_3 microcrystal obtained by SC, UP, CP and MH methods.

Refined formula Ag_2SeO_3	**Lattice Parameters (Å)**			**Cell volume (Å^3)**	**R_{Bragg} (%)**	**χ^2 (%)**
	a	**b**	**c**			
Ag_2SeO_3-SC	4.857(9)	10.338(2)	6.957(1)	349.34(8)	3.53	1.55
Ag_2SeO_3-UP	4.860(0)	10.334(5)	6.959(2)	349.49(6)	3.95	1.50
Ag_2SeO_3-CP	4.857(9)	10.340(1)	6.956(9)	349.35(2)	3.70	1.33
Ag_2SeO_3-MH	4.859(9)	10.339(5)	6.956(1)	349.49(9)	3.25	1.26
Ag_2SeO_3-Theo	4.955	10.600	7.129	374.40	-	-
ICSD n° 78-388	4.854(1)	10.332(3)	6.956(2)	348.79(0)	-	-

A representation of the unit cell for the monoclinic Ag_2SeO_3 structure is presented in Fig. 3. This unit cell was modelled using the visualization for electronic and structural analysis (VESTA) program [67,68], version 3, and were modelled using lattice parameters

and atomic positions obtained from the Rietveld refinement data and from the optimized structure of the theoretical calculation (Ag_2SeO_3-Theo). Fig. 3 shows the existence of two types of distorted octahedral polyhedrons for the Ag sites, Ag1 and Ag2, and a trigonal pyramid for the Se site. These polyhedrons, namely, the [AgO_6] and [SeO_3] clusters, respectively, are related to their local coordination and are responsible for the structural and electronic degree of order-disorder in the crystal lattice.

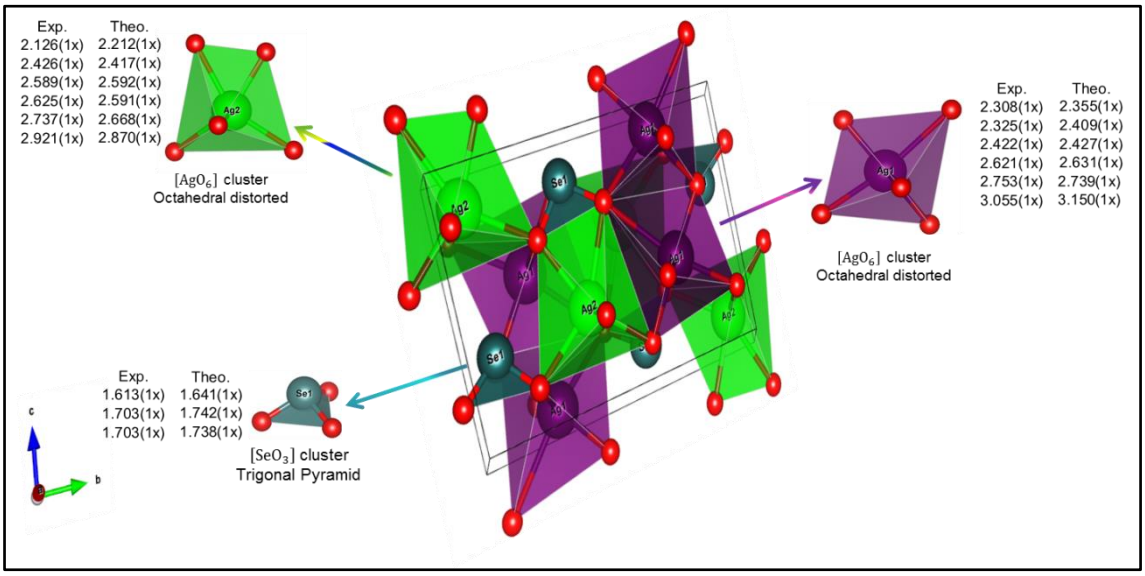

Fig. 3. Schematic representation of the monoclinic Ag_2SeO_3. The two distorted octahedral [AgO_6] clusters and the trigonal pyramid [SeO_3] cluster are highlighted.

XPS

XPS was used to evaluate the surfaces of the Ag_2SeO_3 samples and provide information about chemical composition, binding energy, atomic bonding configuration, electronic structure and oxidation state of the constituent atoms. XPS spectra of the samples are presented in Fig.4, where the C, Ag, Se, and O peaks are clearly observed for the samples and no other elements due to impurities were detected.

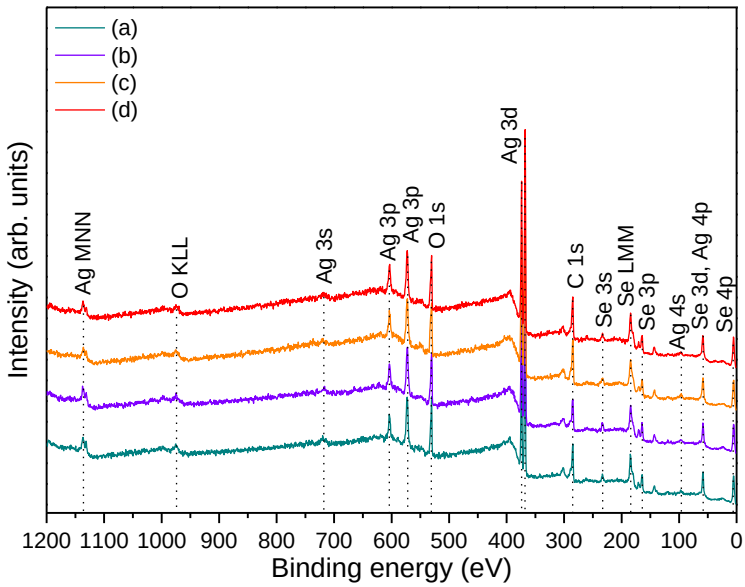

Fig. 4. XPS spectra of the (a) Ag_2SeO_3-SC, (b) Ag_2SeO_3-UP, (c) Ag_2SeO_3-CP, and (d) Ag_2SeO_3-MH samples.

The Ag 3d high-resolution spectra in the range of 380-364 eV show two peaks, as presented in Figs. SI-2(a-d). Two deconvolution components located around 367.5 and 373.5 eV (Δ = 6 eV) are ascribed to Ag $3d_{5/2}$ and Ag $3d_{3/2}$, respectively, confirming the presence of the Ag^+ ion. Two deconvolution components identified around 368.4 and 374.4 eV (Δ = 6 eV) are due to the presence of Ag^0 that can be attributed to the surface coating of Ag nanoparticles on the materials [69–73]. The Se 3d high-resolution spectra in the range of 70-52 eV is shown in Figs. SI-3(a-d). The Se 3d peak has overlapping spin-orbit components (Δ = 0.86 eV, intensity ratio = 0.735). As stated by previous studies, the doublet Se 3d peak around 58.47 eV (Se $3d_{5/2}$) and 59.33 eV (Se $3d_{3/2}$) is attributed to Se (IV) oxidation state [74,75]. The O 1s high resolution spectra in the range of 540-527 eV are presented in Figs. SI-4(a-d), which shows three main spin-orbit components around 530.6, 532.1, and 533.6 eV. In general, the component located at 530.6 is regarding to lattice oxygen, which corresponds to Ag–O and Se–O bonds, related to the host lattice of the materials. The component at 532.1 eV corresponds to the oxygen vacancies and the component at 533.6 eV is regarding to OH groups and water adsorbed on the surface of the materials. [76–82] Therefore, all of these results confirm the existence of Ag, Se, and O elements as well as the purity of the samples. Table SI-3 lists the XPS elements positions and concentration of the area components for Ag, Se and O of the Ag_2SeO_3 samples.

Raman

The structural order in the short range for the Ag_2SeO_3 samples were determined by Raman spectroscopy. According to factor group analysis, the *P2₁/c* structure of Ag_2SeO_3 presents 72 modes, as stated by the following irreducible representation: $\Gamma = 18A_g + 18A_u + 18B_g + 18B_u$. Fig. 5 shows the Raman spectra of Ag_2SeO_3 samples excited at 633 nm. The experimental and calculated vibrational bands of Ag_2SeO_3 are listed in Table 2. Clearly, intense and defined Raman modes are found at 63, 135, 153, 239, 380, 401, 438, 670, 683, 704, and 760 cm^{-1}, which can be assigned to the A_g, A_g, B_g, A_g, A_g, B_g, B_g, A_g, B_g, B_g, and A_g modes, respectively.

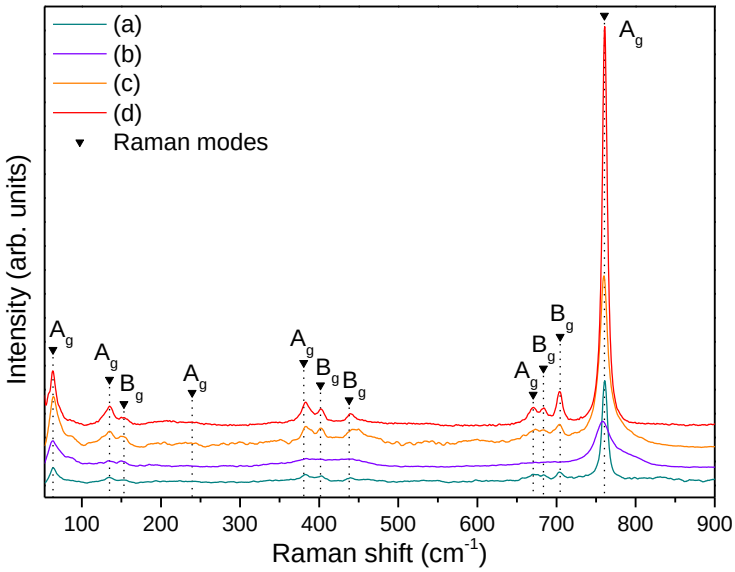

Fig. 5. Raman spectra of the (a) Ag_2SeO_3-SC, (b) Ag_2SeO_3-UP, (c) Ag_2SeO_3-CP, and (d) Ag_2SeO_3-MH samples.

FTIR

The FTIR spectra in the 4000-400 cm^{-1} range of Ag_2SeO_3 samples are presented in Fig. 6. The characteristic bands of to SeO_3 units with C_{3v} point symmetry at 430, 675, 750, and 815 cm^{-1} can be sensed. The bands at 675 cm^{-1}, 750 cm^{-1}, and 815 cm^{-1} correspond to the symmetric and asymmetric stretching modes of Se-O, while O-Se-O bending mode is observed at 430 cm^{-1}.[60,83] The 900-4000 cm^{-1} region of the spectra present bands characteristic of CO_2 and H_2O arising from the room atmosphere and humidity. The symmetrical stretch of carboxylate group can be ascribed to the band identified at 1340 cm^{-1}. The bending vibration band of molecular H_2O appears at 1650 cm^{-1}. The modes at 2360 cm^{-1} and 2340 cm^{-1} and a large mode centered at 3200 cm^{-1} is

related to O-H stretching modes of the adsorbed H_2O. [84–87] The experimental and calculated IR bands of Ag_2SeO_3 are also listed in Table 2.

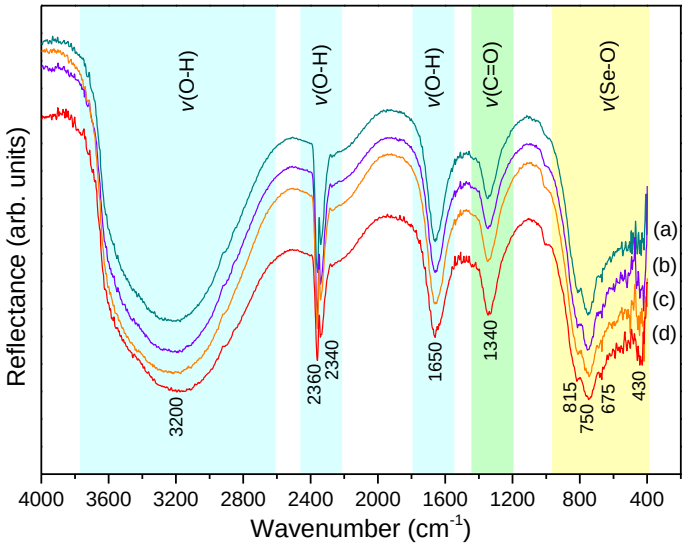

Fig. 6. FTIR spectra at room temperature of the (a) Ag_2SeO_3-SC, (b) Ag_2SeO_3-UP, (c) Ag_2SeO_3-CP, and (d) Ag_2SeO_3-MH samples.

Table 2. Experimental and theoretical values of the Raman and IR vibrational modes of Ag_2SeO_3.

Position (cm^{-1})					
Raman			**IR**		
Modes	**Experimental**	**Theoretical**	**Modes**	**Experimental**	**Theoretical**
A_g	63	58	A_u	430	426
A_g	135	134	B_u	675	666
B_g	153	145	B_u	750	758
A_g	239	247	A_u	815	764
A_g	380	381	-	-	-
B_g	401	391	-	-	-
B_g	438	440	-	-	-
A_g	670	668	-	-	-
B_g	683	686	-	-	-
B_g	704	719	-	-	-
A_g	760	763	-	-	-

FE-SEM

FE-SEM images of Ag_2SeO_3 samples are shown in Fig. 7(a-l). All samples present irregular cub-like rods microparticles of different width and length sizes, in the range of 50-800 nm and 1-15µm, respectively. They are agglomerated and present polydisperse size distribution and shape. As shown in the Fig. 7, the particles present smooth surface and well-defined morphology. Figure 7 (c, f, i, and l) also shows the correspondent planes values obtained by DFT calculations which were responsible for the morphologies experimentally observed.

An analysis of the FE-SEM images for the Ag_2SeO_3-SC microcrystals shown in Fig. 7(a-c) show several elongated rod-like structures, and it is possible to state that microcrystals present a well-defined face-squared and face-rectangular shapes. Fig. 7(d-f) shows the Ag_2SeO_3-UP particles of similar morphology, but the average size of these particles is smaller than the Ag_2SeO_3-UP microcrystals. Drastic reduction on length is observed for the Ag_2SeO_3-CP as it can observed in Fig. 7(g-i). Finally, the Ag_2SeO_3-MH crystals observed in Fig. 7(j-l) present rod/cubic morphologies.

The formation of these particles may involve three main steps: self-aggregation, Ostwald ripening (OR) and self-organization. The OR occurs when the medium attain an equilibrium condition among the solubility and precipitation processes. It happens when small particles in suspension redissolve and are deposited into larger ones. Moreover, this process can arise in two steps: a very slow or fast nucleation step, leading to the formation of polydisperse or monodisperse particles, respectively. [88]

Fig. 7(a-c) display the Ag_2SeO_3 crystals obtained when the SC method is used. The crystals have a rod like flat and elongated shape. The size distribution of the particles, can be related with the crystal sizes that are big enough to be comparable with the ones of the cavitation bubbles. [89] Thus, the longer crystallite fragment are observed. Similar qualitative results were obtained for rod shape obtained along UP method as depicted in Fig. 7(d-f). Fig. 7(g-i) show the morphology of the product obtained by the CP method. It is possible to observe different crystals, some representing a rod like short shape, and the other being nanocrystals formed through crystallographic alignment of the one along a specific crystal surface. The junctions and defects observed in these morphologies, such as twins and staking faults, are a direct evidence of the oriented attachment (OA) growth mechanism. [90,91] FE-SEM images presented in Fig. 7(j-l) correspond to sample for Ag_2SeO_3 crystals obtained by MH and have a hexagonal corner-truncated morphology.

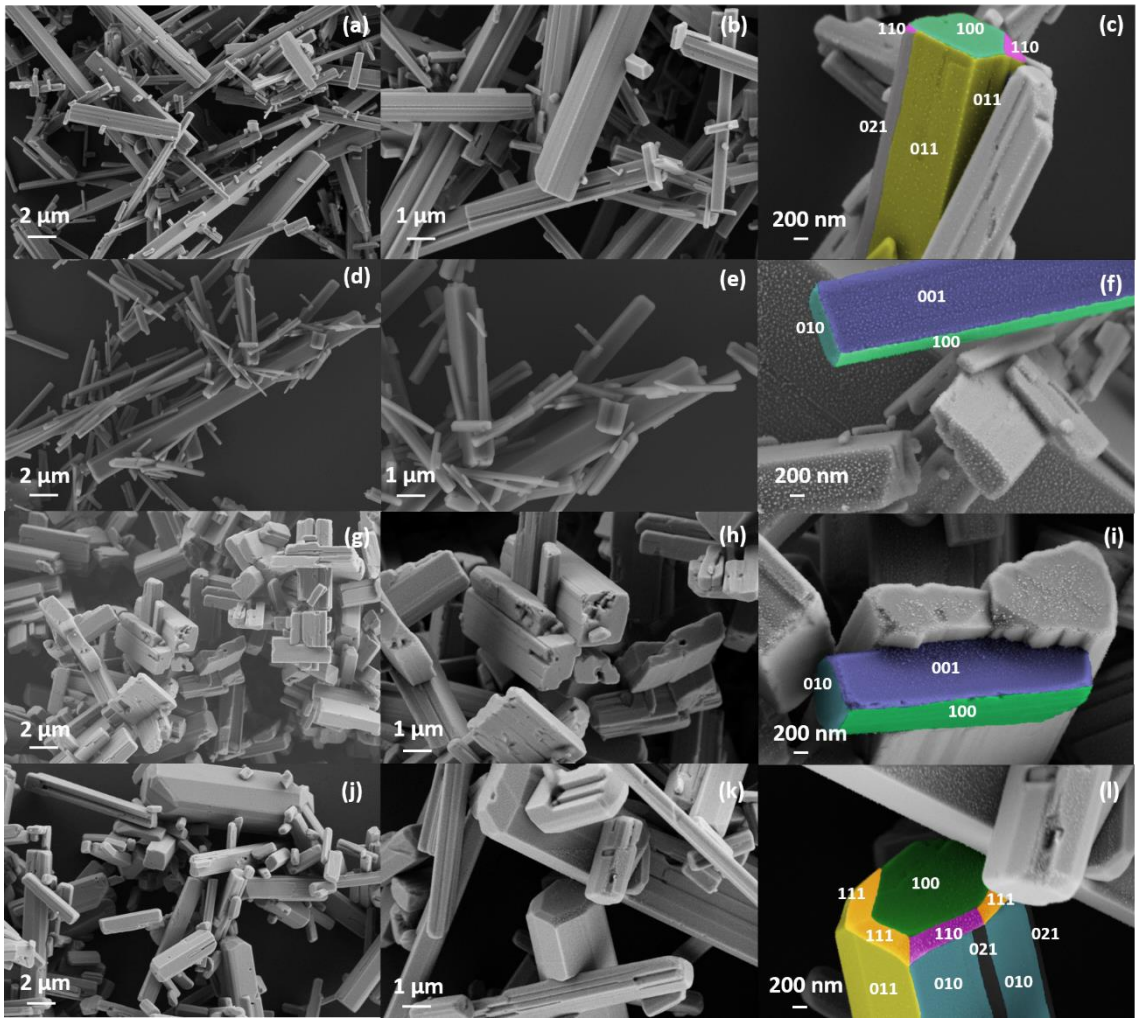

Fig. 7. FE-SEM images of the (a-c) Ag_2SeO_3-SC, (d-f) Ag_2SeO_3-UP, (g-i) Ag_2SeO_3-CP, and (j-l) Ag_2SeO_3-MH samples.

Theoretical results

Surfaces

The mechanism of the morphological transformation and the properties of the monoclinic Ag_2SeO_3, at the atomic level, were performed by DFT calculations to calculate E_{surf} of the (100), (010), (001), (110), (101), (011), (021) and (111) surfaces modeled through of an unreconstructed slab model containing 12, 10, 10, 12, 10, 12, 16 and 16 molecular units, respectively. All possible stoichiometric terminations of each surface were tested, and the optimized surface structure of stable terminations with the lowest value of E_{surf} are shown in Fig. 8.

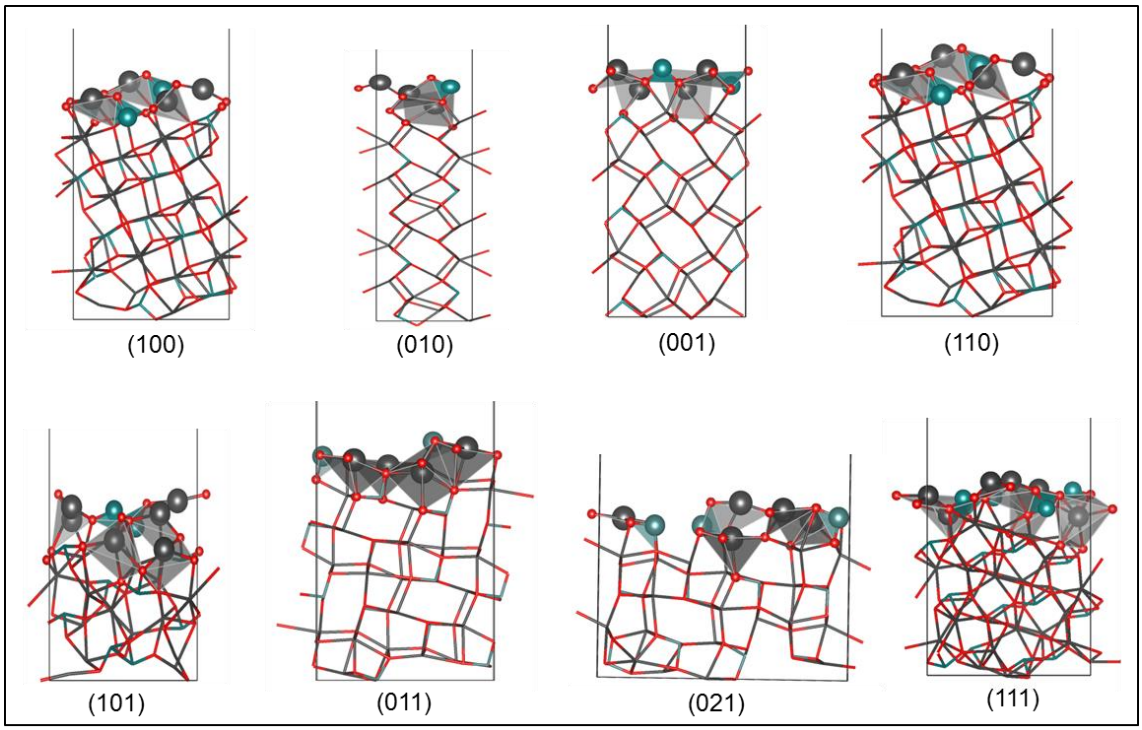

Fig. 8. Structure of the (100), (010), (001), (110), (101), (011), (021) and (111) surfaces based on slab models. Gray, dark cyan and red balls represent Ag, Se and O atoms, respectively. The more superficial Ag and Se clusters are also shown in each surface.

The superficial clusters at the (100), (010), (001), (110), (101), (011), (021) and (111) surfaces of Ag_2SeO_3 are presented in Table 3. The vacancies of O atoms (V_O^x) of the Ag clusters are classified by using the Kronger-Vinger notation.[92] It is important to note that all considered surfaces are Ag, Se and O terminated, with Ag atoms incompletely coordinated ($[AgO_y]_d$ with $y = 2,\ 3,\ 4,\ 5$) whereas the Se atoms are fully coordinated when compared with the clusters of Se atom in the bulk, i.e., during the slab construction process on each surface, no Se−O bond is broken and the $[SeO_3]$ cluster is maintained.

Table 3. The clusters at the (100), (010), (001), (110), (101), (011), (021) and (111) surfaces of Ag_2SeO_3. The vacancies of O atoms in the Ag clusters are indicated by using the Kronger-Vinger notation.

Surfaces	***Clusters***
(100)	$[AgO_4 \cdot 2O], [AgO_5 \cdot O]\ and\ [SeO_3]$
(010)	$[AgO_2 \cdot 4O], [AgO_5 \cdot O], [AgO_6]_d\ and\ [SeO_3]$
(001)	$[AgO_4 \cdot 2O], [AgO_5 \cdot O], [AgO_6]_d\ and\ [SeO_3]$
(110)	$[AgO_2 \cdot 4O], [AgO_4 \cdot 2O], [AgO_5 \cdot O]\ and\ [SeO_3]$
(101)	$[AgO_2 \cdot 4O], [AgO_3 \cdot 2O], [AgO_4 \cdot O]\ and\ [SeO_3]$
(011)	$[AgO_5 \cdot O], [AgO_6]_d\ and\ [SeO_3]$
(021)	$[AgO_3 \cdot 3O], [AgO_4 \cdot 2O], [AgO_5 \cdot O]\ and\ [SeO_3]$
(111)	$[AgO_3 \cdot 3O], [AgO_4 \cdot 2O], [AgO_5 \cdot O], [AgO_6]_d\ and\ [SeO_3]$

The stability order of the surfaces decreases as follows: $(011) > (100) > (001) > (021) > (110) > (111) > (010) > (101)$ (Table 4). The (011) displays the lower number of broken bonds. The (001) and (010) surfaces exhibit the same number broken bonds, however (001) surface showed higher stability than (010) surface. By analyzing the structure of each surface, it can be noted that $[AgO_5 \cdot O], [AgO_6]_d\ and\ [SeO_3]$ clusters are common in both surfaces, however, while (001) surface present $[AgO_4 \cdot 2O]$ clusters, (010) surface present $[AgO_2 \cdot 4O]$ clusters as well as area smaller than (001) surface. These two characteristics mean that the chemical environment is different on the two surfaces and that the interatomic interactions become more important on the (010) surface, making it more unstable.

Table 4. Calculated surface energy values (E_{surf}), energy band gap (E_{gap}), broken bonds (N_b), $Area$, broken bond density (D_b) for (011), (100), (001), (021), (110), (111), (010) and (101) surfaces of Ag_2SeO_3.

Surfaces	$E_{surf}\,(Jm^{-2})$	$E_{gap}\,(eV)$	$Area(nm^2)$	N_b	$D_b(nm^{-2})$
(011)	0.23	3.56	0.6327	3	4.74
(100)	0.24	3.74	0.7558	6	7.94
(001)	0.30	3.62	0.5284	5	9.46
(021)	0.35	3.37	0.8804	9	10.22
(110)	0.36	3.73	0.8343	9	10.79
(111)	0.37	3.74	0.9908	12	12.11
(010)	0.64	3.60	0.3534	5	14.15
(101)	0.70	2.94	0.9257	16	15.12

To further compare the electronic properties of the eight surfaces, the band structure of (011), (100), (001), (021), (110), (111), (010) and (101) surfaces are plotted in Fig. 9. The results reveal that the (100), (110) and (111) surfaces show a E_{gap} around 3.74 eV, slightly higher that the E_{gap} of the bulk, whereas (001) and (010) surfaces with E_{gap} of 3.62 and 3.60 eV, respectively, very close to the calculated E_{gap} of 3.64 eV for bulk Ag_2SeO_3. On the other hand, the lower E_{gap} of 3.56, 3.37 and 2.94 eV were observed for the (011), (021) and (101) surfaces, respectively. The DOS of (011), (100), (001), (021), (110), (111), (010) and (101) surfaces are plotted in Fig. 10. The composition of the VB and CB are the same as that in bulk of Ag_2SeO_3, with contributions of O 2*p* and Ag 4*d* orbitals at the VB and Se 4*p*, Ag 5*s*5*p* and O 2*p* orbitals for the CB. In (100), (001), (021), (110), (111), (010) surfaces the dispersion of the valence band is smaller in comparison with the bulk while the CB in these surfaces show similar characteristic that observed for the bulk. On the other hand, both VB maximum and the CB minima in (101) surface are flat and more disperse in comparison with the bulk. Besides, in the region of VB (0.5 to 0 eV) and CB (2.0 to 2.5 eV), the DOS of the (011) surface is more localized than that of the (010) surface.

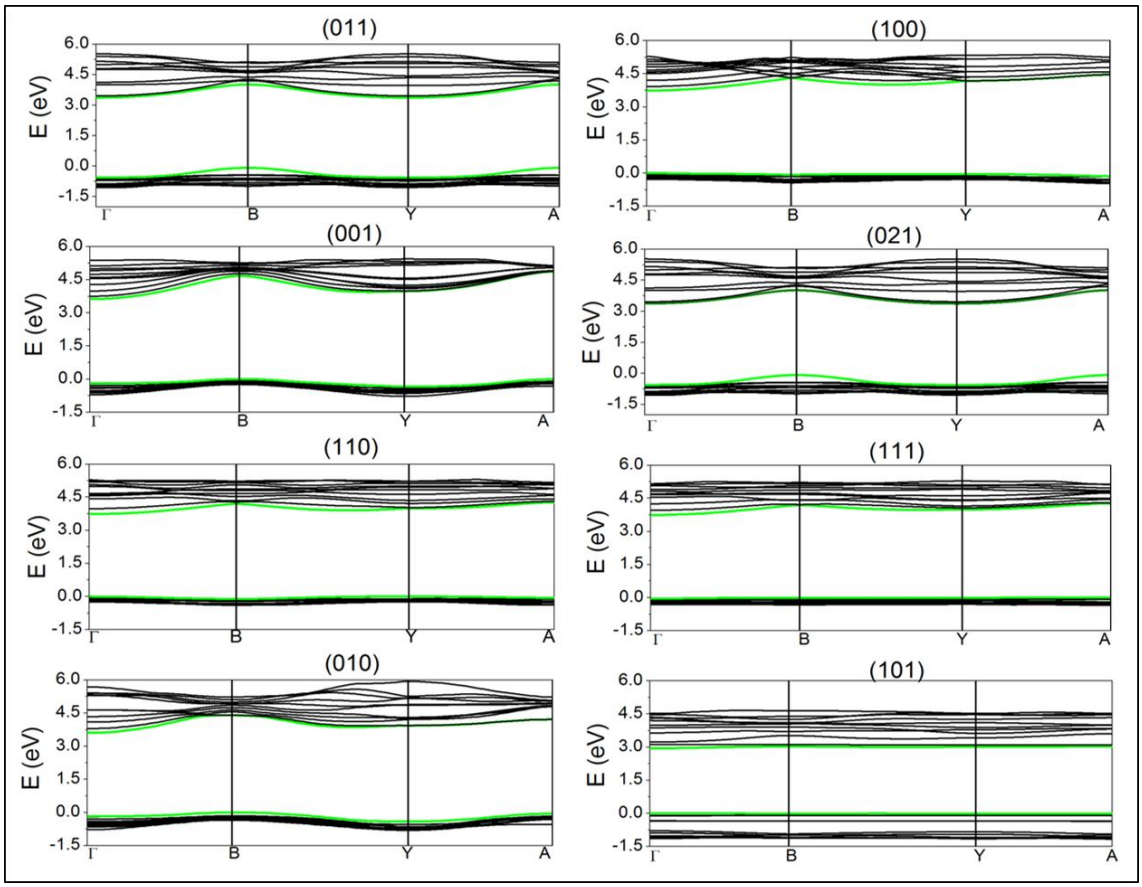

Fig. 9. Band structure for the (011), (100), (001), (021), (110), (111), (010) and (101) surfaces of Ag_2SeO_3.

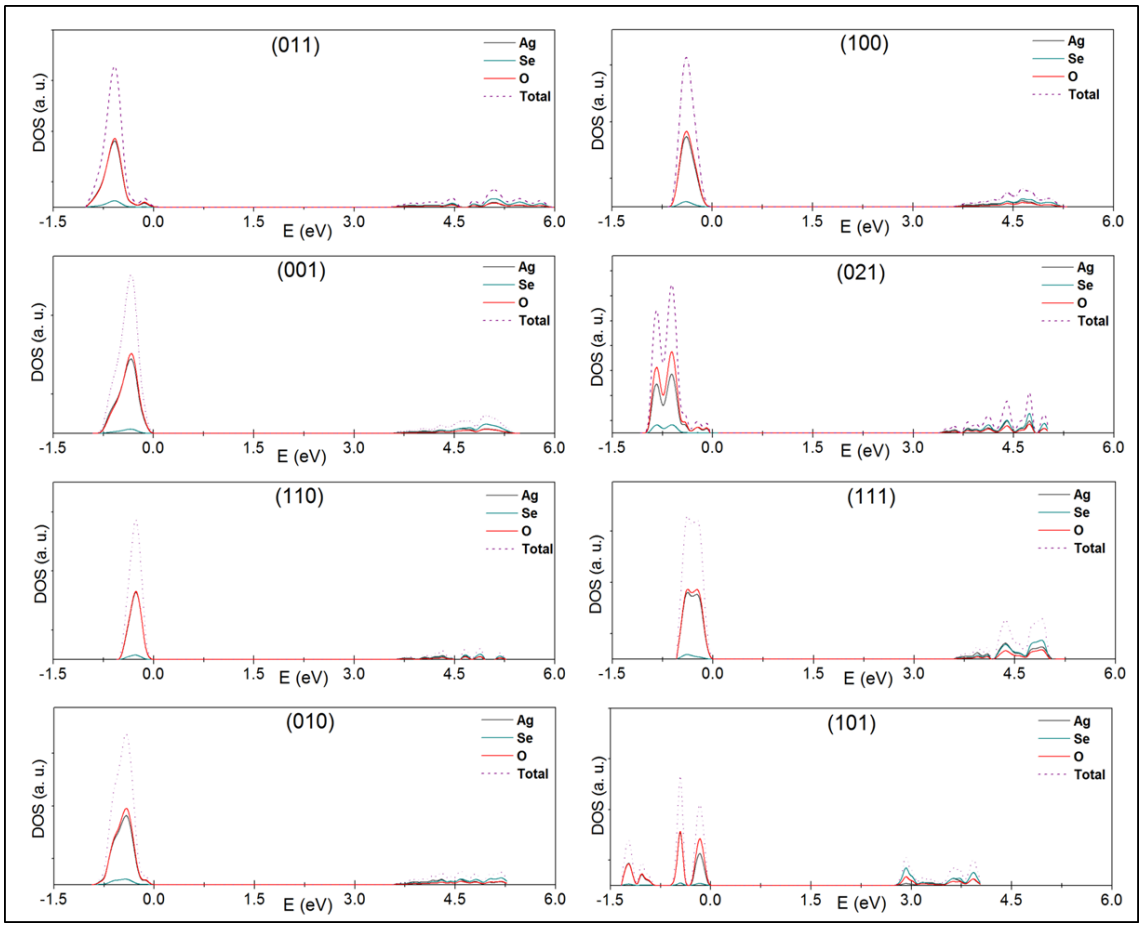

Fig. 10. DOS for the (011), (100), (001), (021), (110), (111), (010) and (101) surfaces of Ag_2SeO_3.

Morphology

Considering the experimental results shown in Fig. 7, the theoretical calculations were performed to rationalize the morphologies of Ag_2SeO_3 obtained by means of the different synthesis methods. The ideal Wulff's representation of the optimized Ag_2SeO_3 exhibited a cubic corner-truncated shape with the (011) and (100) surfaces predominantly exposed and in minor extent the (110) surface. Furthermore, assuming different values of the E_{surf} for the different surfaces, a complete map of available morphologies that are compared with the experimental FE-SEM images are illustrated in Fig. 11.

The formation of Ag_2SeO_3-SC, Ag_2SeO_3-UP and Ag_2SeO_3-CP samples comprises two processes which could be related to the OA process: (i) the formation of small Ag_2SeO_3 nanoparticles as the primary crystal nuclei which exhibited an elongated cube with the exposed (100), (001) and (010) surfaces (A1 shape in Fig.11); and (ii) the subsequent crystal growth to form single-crystalline Ag_2SeO_3. Under ultrasound

conditions the stabilization of the (101) surface is favored which leads to the flat primary particles (A2 in Fig. 11). The OR process of the primary particles A2 is believed to occur by the coalescence, leading to the formation of A3 crystal (See Fig. 11). The FE-SEM images of Ag_2SeO_3-SC and Ag_2SeO_3-UP (Fig. 7(a-c) and 7(d-f) confirm a change in the size and shape of the particles, i.e., the particles initially formed grow preferentially in the (010) direction to form elongated and flat structure). In the case of the Ag_2SeO_3-CP the interaction between the primary particle units occur through of (001) surface of the A1 shape, as marked by a double arrow in Fig. 11, leading to the formation of a monocrystal.

On the other hand, when the MH radiation is used, the primary crystal nuclei (B1 shape in Fig. 11) is a hexagonal corner-truncated shape with the more exposed (011) and (111) surfaces and, in minor extent, the exposed (021) and (010) surfaces. The MH method promotes the appearance of the unstable (010) and (111) surfaces, derived from the destabilization of (100) and (110) surfaces with subsequent growth of crystal in the direction (100) to get to render the B2 morphology, and finally, by the stabilization of (021) surface the B3 shape is obtained.

Fig. 12 displays two reaction paths constructed from the calculated E_{poly} values (Table SI-4). The reaction path A corresponds to a process that goes through a high energy intermediate (A1) until it reaches the final morphologies (A2 and A3) which showed a rather similar stability to the ideal Ag_2SeO_3 morphology. Along the reaction path B, morphologies with higher E_{poly} were obtained (B2 and B3).

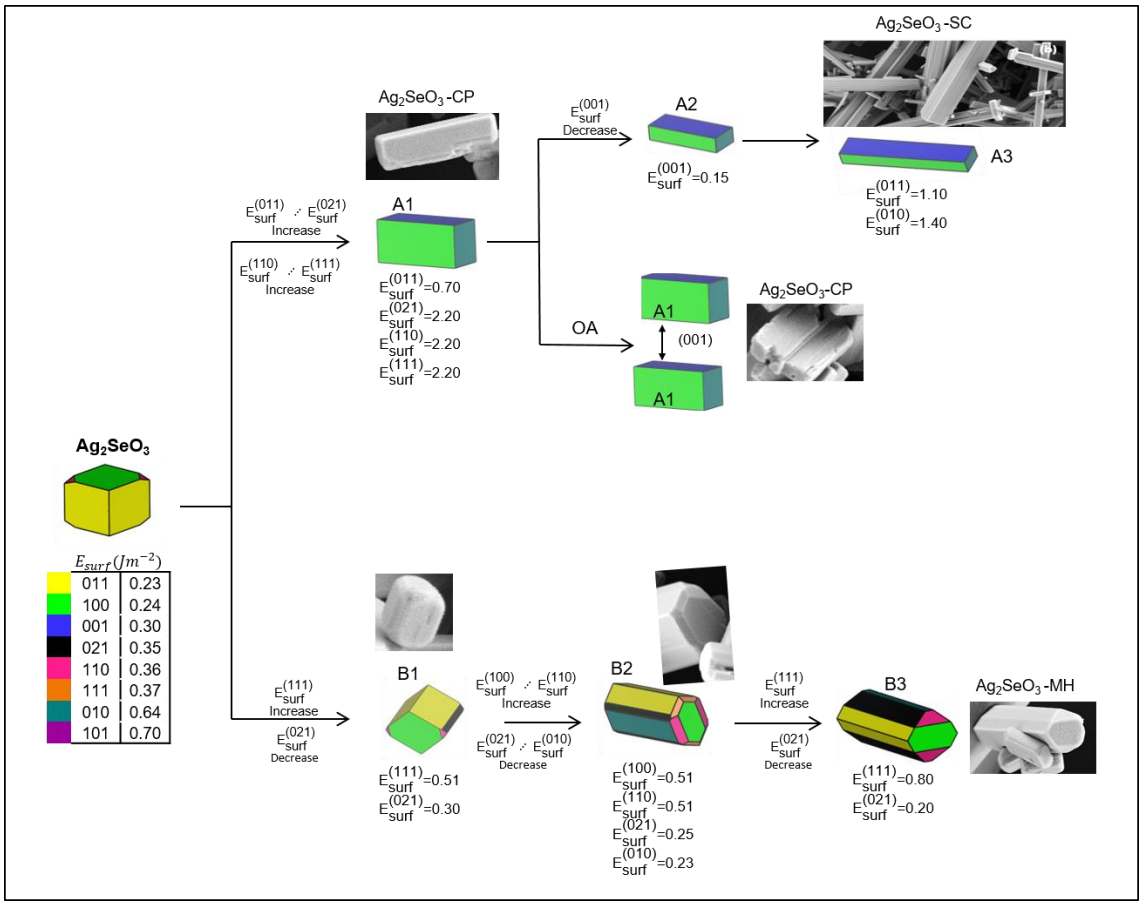

Fig. 11. Schematic illustration of the morphologies obtained by tuning of the E_{surf} of (011), (100), (001), (021), (110), (111), (010) and (101) surfaces of Ag_2SeO_3.

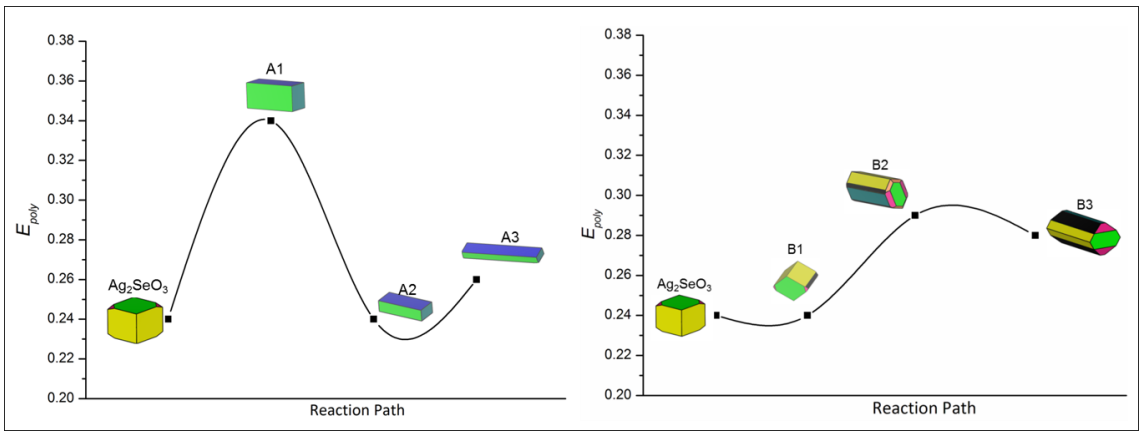

Fig. 12. The polyhedron energy, E_{poly}, is plotted versus the corresponding reaction path.

UV-vis spectroscopy

Fig. 13(a-d) illustrate the UV-vis diffuse reflectance spectra of the Ag_2SeO_3 samples within the range of 300-800 nm. The samples presented absorption in the

ultraviolet range of approximately 350 nm. The absorption arises from electronic transition between the VB formed by the hybridization of the Ag 4*d* orbitals and the O 2*p* orbitals, and the CB which has major contributions from the Ag 5*s* orbitals and the Se 4*p* orbitals.

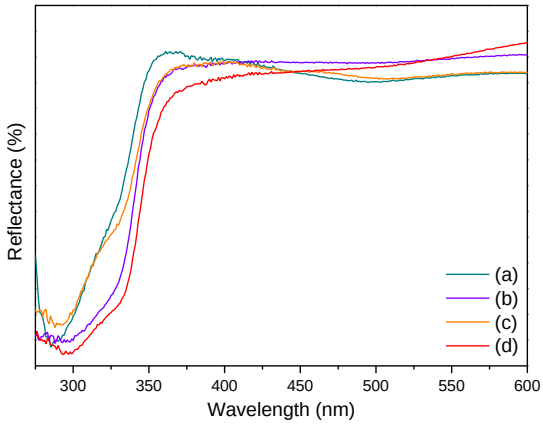

Fig. 13. UV-vis diffuse reflectance spectra of the (a) Ag_2SeO_3-SC, (b) Ag_2SeO_3-UP, (c) Ag_2SeO_3-CP, and (d) Ag_2SeO_3-MH samples.

The band gap energy (E_{gap}) values were acquired by linear extrapolation of the UV-vis curves in the $[F(R_\infty)h\nu]^n$ *versus* $h\nu$ graph, which were calculated using the relation of the Kubelka-Munk and Wood Tauc function [93,94]. $F(R_\infty)$ is the Kubelka-Munk function, $h\nu$ is the photon energy, and n is a constant related to the type of electronic transition of a semiconductor, with n = 0.5 for direct allowed, n = 2 for indirect allowed, n = 1.5 for direct forbidden, and n = 3 for indirect forbidden. The theoretical calculation predicts an indirect allowed transition for Ag_2SeO_3 with the $P2_1/c$ space group, which accounts for n = 2. The E_{gap} values obtained were 3.54, 3.59, 3.44, and 3.52 for the Ag_2SeO_3-SC, Ag_2SeO_3-UP, Ag_2SeO_3-CP, and Ag_2SeO_3-MH samples, respectively (see Fig. SI-5). These results show a slight decrease in the E_{gap} of Ag_2SeO_3 obtained by CP method with respect to that obtained with SC, UP and MH methods. It is believed that CP method can generate a high degree of structural defects (short, medium and long range) which can be a consequence of interparticle interactions in the crystal growth process. Under the other synthesis conditions, radiation causes a reduction of structural defects in the Ag_2SeO_3 crystals, which is evidenced by the higher in E_{gap} values.

The band structure of Ag_2SeO_3 monoclinic was calculated by DFT/B3LYP. The band gap energy theoretically estimated (3.64 eV) is in the range of the experimental

values (3.54, 3.59, 3.44, and 3.52 eV for the Ag_2SeO_3-SC, Ag_2SeO_3-UP, Ag_2SeO_3-CP, and Ag_2SeO_3-MH samples, respectively).

As depicted in Fig. 14, the top of the VB is located in the B point and the bottom of the CB is located in the Γ point on the first Brillouin zone. This implies that Ag_2SeO_3 is an indirect band gap semiconductor. As shown in Fig. 14, the CB of Ag_2SeO_3 is constructed by the *Ag 5s*, *Se 4p* and *O 2p* orbitals whereas the VB is constructed by the hybridized orbitals (*O 2p* + *Ag 4d*). In effect, these hybridized orbitals (O 2*p* + Ag 4*d*) have already been related in others previously reported Ag-containing photocatalysts, and usually lead to absorption of visible light. [42,95]. More specifically the VB is formed by the Ag $4d_{yz}$, $4d_z^2$ orbitals and O $2p_z$ and the CB by the Se $4p_z$ and $4p_x$ orbitals and the O $2p_z$ orbitals.

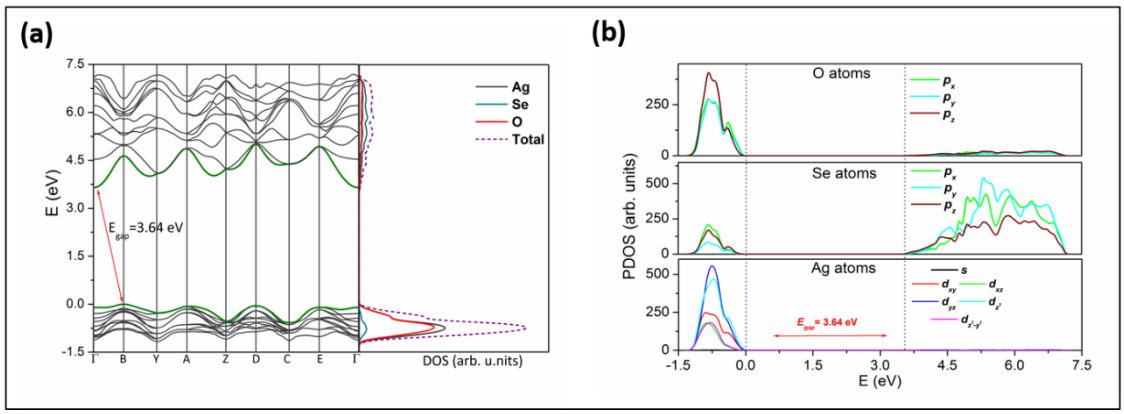

Fig. 14. (a) Structure band and DOS and (b) PDOS of Ag_2SeO_3 calculated by DFT.

Photoluminescence emissions

Fig. 15(a-d) display the PL spectra of Ag_2SeO_3 samples under the excitation wavelength of 355 nm. All samples present a broadband profile covering the region of 550-950 nm, with maximum PL intensity at 689 nm. This behaviour is due to the radiative transition within the octahedral [AgO_6] cluster. Moreover, this PL profile is related to structural and electronic defects of the *[SeO_3]* and *[AgO_6]* clusters, and is similar to other selenite matrices. Emissions in the red region have also been reported in others Ag-containing photocatalysts, and are associated with the distorted and undercoordinated clusters at the exposed surfaces, which induce structural disorder and deeper defects in the band gap region. Among the samples, it was noted that the Ag_2SeO_3-SC sample had

the lowest PL intensity, associated to a lower recombination rate of electron-hole (e′─h•) pairs compared to the other samples. [96]

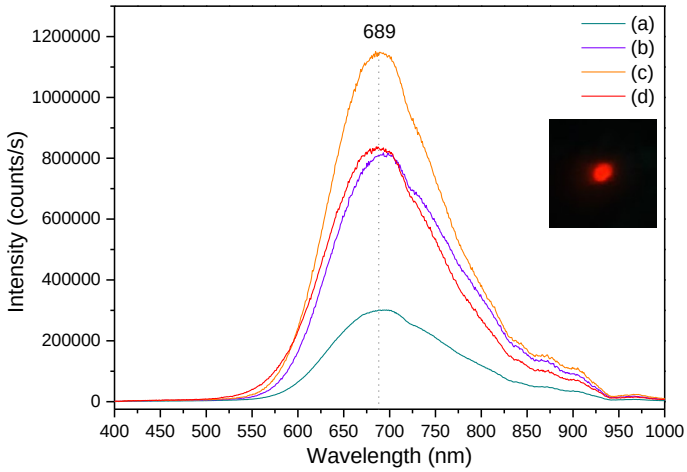

Fig. 15. PL emissions of the (a) Ag_2SeO_3-SC, (b) Ag_2SeO_3-UP, (c) Ag_2SeO_3-CP, and (d) Ag_2SeO_3-MH samples. Inset: corresponding optical image of the Ag_2SeO_3-CP sample under laser illumination.

Fig. 16 shows the deconvolution of the PL emissions for the Ag_2SeO_3 samples. The Voigt area G/L function was used for the deconvolution process, resulting in three components centred at 680 nm, 766, and 876 nm for all samples. An analysis of the results shows that the Ag_2SeO_3-CP and Ag_2SeO_3-MH samples have a larger percentage of emission for the 680 nm component. The longer wavelength region of the PL spectra can be related to the presence of vacancy defects and shorter wavelength region is ascribed to intrinsic structural defects. Thus, these samples may present larger numbers of defects, which generate intermediate energy levels between the VB and CB.

Fig. 17 shows the CIE chromatic diagram and the respective positions of x, and y coordinates of the Ag_2SeO_3 samples obtained through the PL emission spectra. The (x;y) chromatic coordinates positions are located at Ag_2SeO_3-SC (0.72;0.28), Ag_2SeO_3-UP (0.72;0.28), Ag_2SeO_3-CP (0.71;0.28), and Ag_2SeO_3-MH (0.71;0.28). All samples present intense emitting colour in the red region, and the (x;y) coordinates are all located near the red edge of diagram, confirming the pureness and brightness of the emitted colour. These results are promising to apply these materials as optical devices.

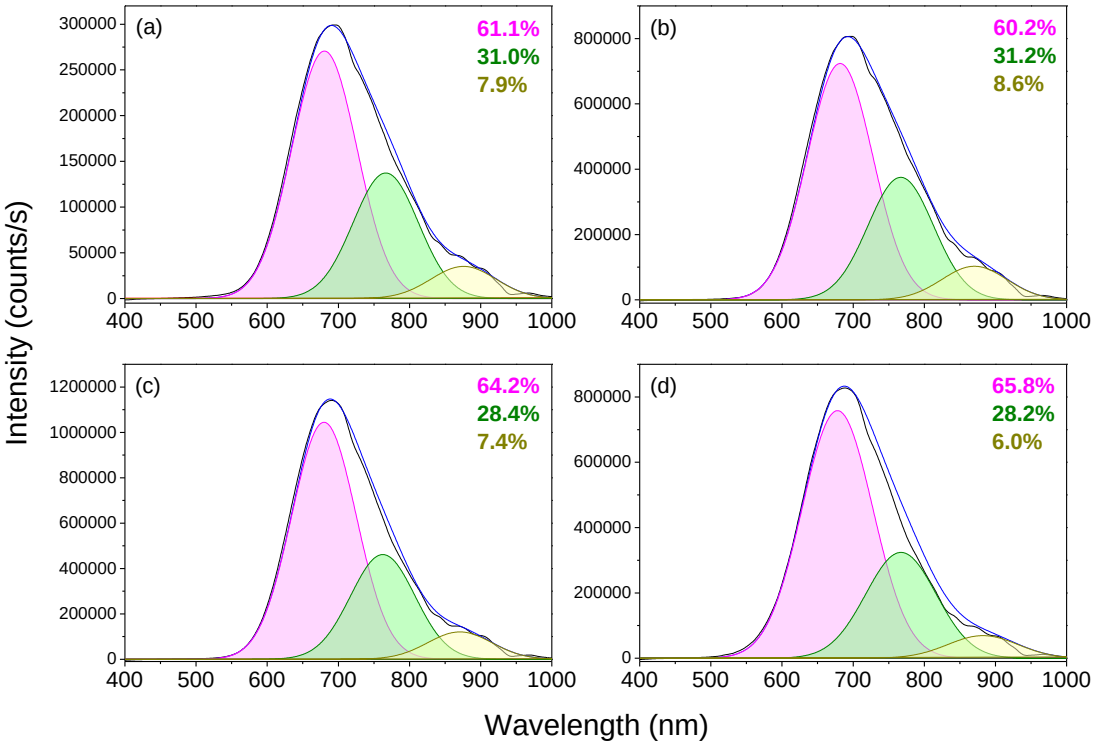

Fig. 16. PL deconvolution spectra of (a) Ag_2SeO_3-SC, (b) Ag_2SeO_3-UP, (c) Ag_2SeO_3-CP, and (d) Ag_2SeO_3-MH samples. Inset: Percentage of colour area for the components.

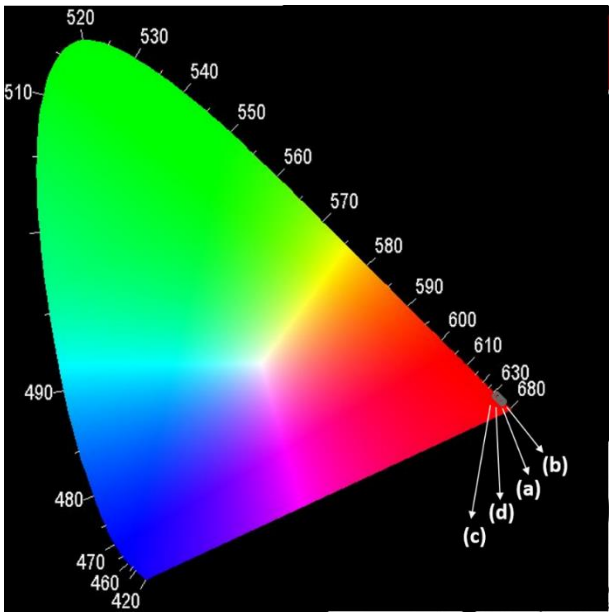

Fig. 17. CIE chromatic diagram of (a) Ag_2SeO_3-SC, (b) Ag_2SeO_3-UP, (c) Ag_2SeO_3-CP, and (d) Ag_2SeO_3-MH samples.

Photocatalytic activity

Photocatalytic tests of Ag_2SeO_3-SC, Ag_2SeO_3-UP, Ag_2SeO_3-CP and Ag_2SeO_3-MH samples were performed under UV light irradiation for photodegradation of RhB. The aliquots removed at certain times (0, 2, 5, 10, 20, 30, 40 and 60 minutes) were monitored by spectrophotometry using the RhB maximum absorption wavelength (λ_{max} = 554 nm). The absorbance spectra are shown in Fig.18(a-d) where it is observed that all samples show photocatalytic activity for RhB degradation.

In a similar work, Yang et al. [97] related the photocatalytic activity of TiO_2 (P25) using RhB dye and UV light irradiation. It was observed that in 30 minutes of irradiation, approximately 90% of the dye is degraded, however the UV lamps used have a power of 500W, about 8 times the power used in our study. The mass of the catalyst and RhB concentration are very close to that used in this work, thus, the Ag_2SeO_3 samples, highlighting the Ag_2SeO_3-SC, have very promising photocatalytic activity, degrading all dye in approximately 60 minutes of UV light irradiation, using only 60W of power.

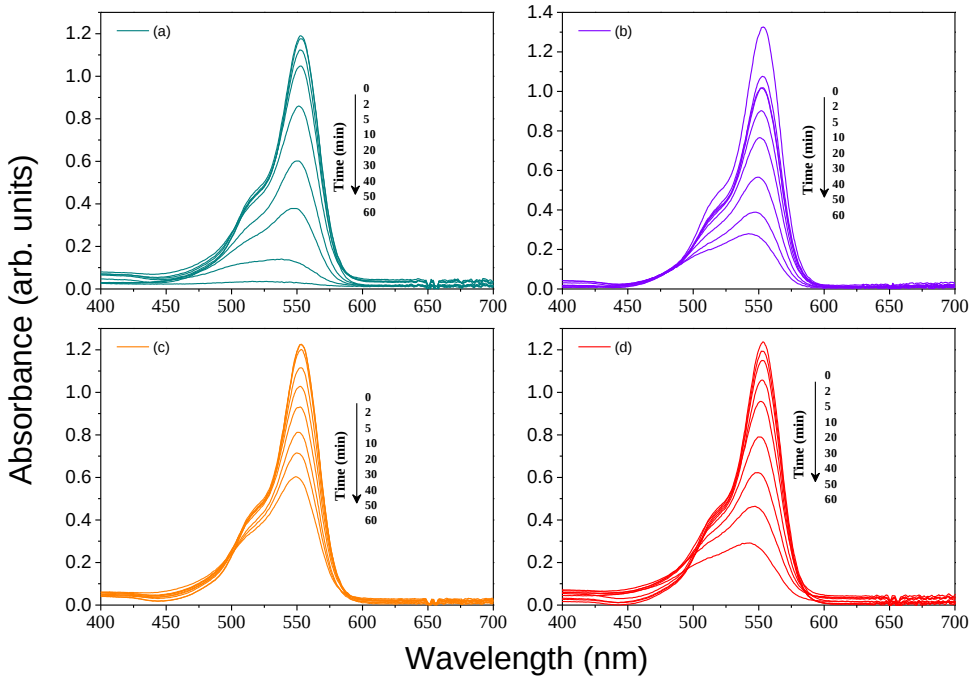

Fig. 18. UV–vis absorption spectra of RhB upon photodegradation in the presence of (a) Ag_2SeO_3-SC, (b) Ag_2SeO_3-UP, (c) Ag_2SeO_3-CP, and (d) Ag_2SeO_3-MH samples.

Fig. 19(a) shows the relative absorbance of each sample as function of irradiation time (t), with A_0 being the absorbance at time 0, after the adsorption-desorption period and A being the absorbance at certain times of UV light irradiation. Note that the Ag_2SeO_3-SC sample degraded practically all RhB in about 1 hour of exposure to UV

light. An experiment under the same conditions without the presence of catalysts was performed and is shown in Fig. 19(a). Using a pseudo-first order kinetic model (Langmuir-Hinshelwood) and considering the equation $-\ln(A/A_0) = kt$ [98], it was possible to obtain the reaction rate constant (k) (Fig 19 (b)).

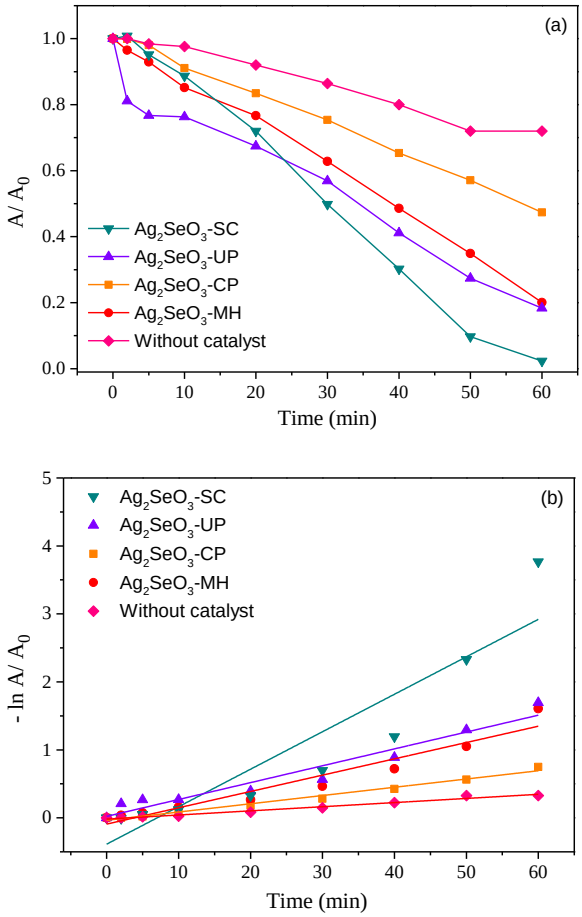

Fig. 19. Photocatalytic degradation of RhB (1.0×10^{-5} mol/L) in the absence and in the presence of different photocatalysts (a) and in log plot for the determination of the rate constant.

Fig. 20 (a) shows the values found for k, being 0.01214, 0.024, 0.0248, 0.05512 and 6.00 x 10^{-3} min^{-1} for Ag_2SeO_3-CP, Ag_2SeO_3-MH, Ag_2SeO_3-UP, Ag_2SeO_3-SC, and without catalyst, respectively, proving that the Ag_2SeO_3-SC sample had the higher photocatalytic activity among the samples, being about 2 times faster than the Ag_2SeO_3-MH and Ag_2SeO_3-UP samples and approximately 4 times faster than the Ag_2SeO_3-CP sample. The photocatalytic activity presented by the Ag_2SeO_3-SC sample can be explained by the lower recombination rate of the e′—h• pairs, as seen in Fig. 15. A lower intensity of PL indicates a lower recombination rate, increasing the availability of the

e′─h• pairs to act in the photodegradation of RhB, both directly and forming the radical species that can also act on photodegradation. The Ag_2SeO_3-CP sample showed the lowest photocatalytic activity and the highest PL intensity, confirming that a higher recombination rate can interfere in the photocatalytic activity of the material, since the e′─h• pairs are not available to act on the degradation of RhB. The Ag_2SeO_3-MH and Ag_2SeO_3-UP samples showed intermediate PL intensities, and consequently their photocatalytic activities were higher than the Ag_2SeO_3-CP sample and lower than the Ag_2SeO_3-SC sample. Another point that can explain the higher photocatalytic activity of the Ag_2SeO_3-SC sample was the change in its particle morphology, which preferably grown in the direction (010), forming an elongated and flat particle, which may have contributed to its photocatalytic response.

In order to understand which radical species are responsible for the degradation process of the RhB dye, radical capture experiments were carried out using tert-butyl alcohol (TBA), ammonium oxalate (AO) and benzoquinone (BQ), respectively, as scavengers of hydroxyl radical (OH*), h•, and superoxide radical (O_2'), respectively. These experiments were carried out under the same conditions as the previous tests and using the Ag_2SeO_3-SC sample, which showed better photocatalytic activity. Fig. 20 (b) shows total inhibition of photodegradation when AO is added, indicating that the h• act directly on the degradation mechanism. When TBA was added, there was a decrease of about 50% in the percentage of degradation, revealing that the OH* species participates to a lesser extent in the degradation process. When adding BQ, there was no change in degradation, revealing that the O_2' species is not participating in this mechanism.

In addition to the excellent photocatalytic efficiency, the reuse and stability of the photocatalyst is of utmost importance and was studied using the Ag_2SeO_3-SC photocatalyst, which showed higher photocatalytic activity. The stability was tested by performing 3 running cycles of RhB photodegradation under UV light irradiation and the results are shown in Fig.20 (c). Note that from the first to the second cycle the material remains stable and in the third cycle the photocatalytic performance shows a slight decrease. This result can be explained by the photodecomposition and formation of Ag^0. [99] Fig.SI-6 shows the XRD of Ag_2SeO_3-SC after the photodegradation cycles, and it is possible to observe a peak at $2\theta = 38.1°$ which corresponds to facet (111) of the cubic Ag^0, confirming the formation of Ag^0 during the photocatalysis process. The Ag^0 formed under the surface of the catalyst prevents the incidence of light, and consequently, reduces the photocatalytic activity of the material. [100] The Ag^0 formed under the Ag_2SeO_3-SC did

not significantly affect the photocatalytic activity, being possible the degradation of approximately 97% of RhB in 1 hour of UV light irradiation, showing that the material developed in this study has a good stability, being possible its reuse.

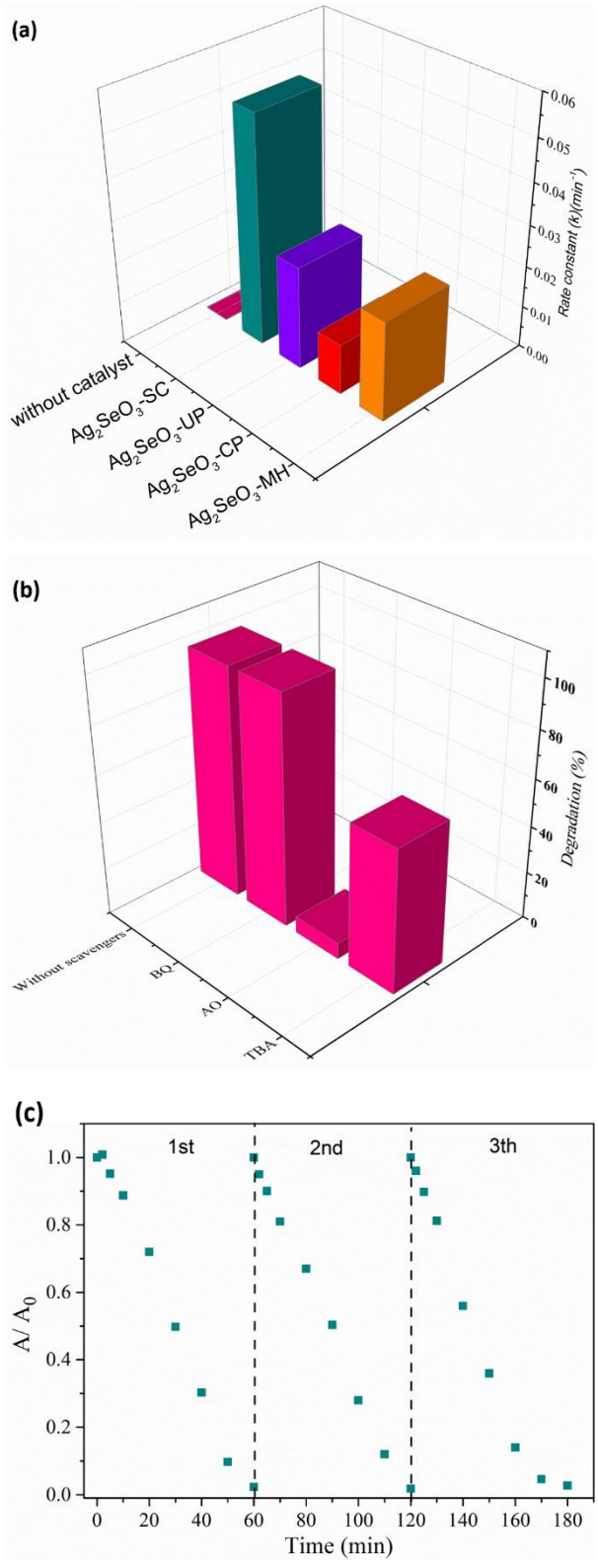

Fig. 20. Degradation rate constants (k) of RhB (a), photocatalytic degradation of RhB using Ag_2SeO_3-SC in the presence of different scavengers under irradiation of UV light (b), and cycling runs for RhB photodegradation over Ag_2SeO_3-SC under UV light irradiation (c).

Photocatalytic mechanism for the degradation of RhB

In order to propose an adequate photodegradation mechanism, an energy band diagram is obtained by calculating the CB and VB potentials of the Ag_2SeO_3-SC sample, using the following empirical equations [101]:

$$E_{VB} = \chi - E_e + 0.5E_{gap}$$
$$E_{CB} = E_{VB} - E_{gap}$$

where E_{VB} is the valence band potential, E_{CB} is the conduction band potential, E_e is the free electron energy on the hydrogen scale (~ 4.5 eV), E_{gap} is the semiconductor band gap energy and χ is the Mulliken's electronegativity of the semiconductor. The χ of Ag_2SeO_3 was calculated from the geometric mean of the electronegativity of the constituent atoms, with the value found being 6.06 eV. Thus, using equations above and the E_{gap} value of 3.54 eV, the E_{VB} and E_{CB} values of 3.33 eV and -0.21 eV were obtained for the Ag_2SeO_3-SC sample.

The proposed degradation mechanism for the Ag_2SeO_3-SC sample was made using the Kröger-Vink notation [92] and is shown in Fig.21. Ag_2SeO_3 is formed by clusters of $[AgO_6]^x$ and $[SeO_3]^x$ with neutral charge. When the material is irradiated by UV light, $[AgO_6]^\bullet$ clusters are formed, with positive charges in VB that act as $h^\bullet$ and $[SeO_3]'$ clusters with negative charge in CB that act as e′, according to the following equation.

$$[AgO_6]^x + [SeO_3]^x + h\nu \rightarrow [AgO_6]^\bullet + [SeO_3]'$$

As seen in Fig. 17 (b), $h^\bullet$ is the predominant species in the photodegradation of RhB, thus the $[AgO_6]^\bullet$ cluster, which acts as $h^\bullet$, may be acting by directly degrading the dye [102], forming colorless organic compounds (COC), water (H_2O), carbon dioxide (CO_2) and $[AgO_6]^x$ cluster, as shown in the equation below.

$$[AgO_6]^\bullet + RhB \rightarrow COC + H_2O + CO_2 + [AgO_6]^x$$

The $[AgO_6]^{\bullet}$ cluster may also be acting in the production of the OH* radical, which had a relevant participation in the photodegradation process. This radical is generated in the VB of Ag_2SeO_3-SC sample, as its potential is higher than for the OH*/H_2O reaction potential (2.70 eV) [103], oxidizing H_2O by the cluster $[AgO_6]^{\bullet}$, and generating OH* and proton $H^{\bullet}$, as shown in the following equation:

$$[AgO_6]^{\bullet} + H_2O \rightarrow OH^* + H^{\bullet} + [AgO_6]^{x}$$

The $[SeO_3]'$ cluster present in CB, acting as e′, reduces the O_2, because the potential of the O_2/ O_2' reaction (-0.046 eV) [104] is higher than CB of Ag_2SeO_3-SC sample.

$$[SeO_3]' + O_2 \rightarrow O_2' + [SeO_3]^{x}$$

However, as seen in Fig.20, the O_2' species does not participate effectively in the photodegradation mechanism. Therefore, the whole mechanism occurs through oxidative pathways, by the $h^{\bullet}$ and OH* species.

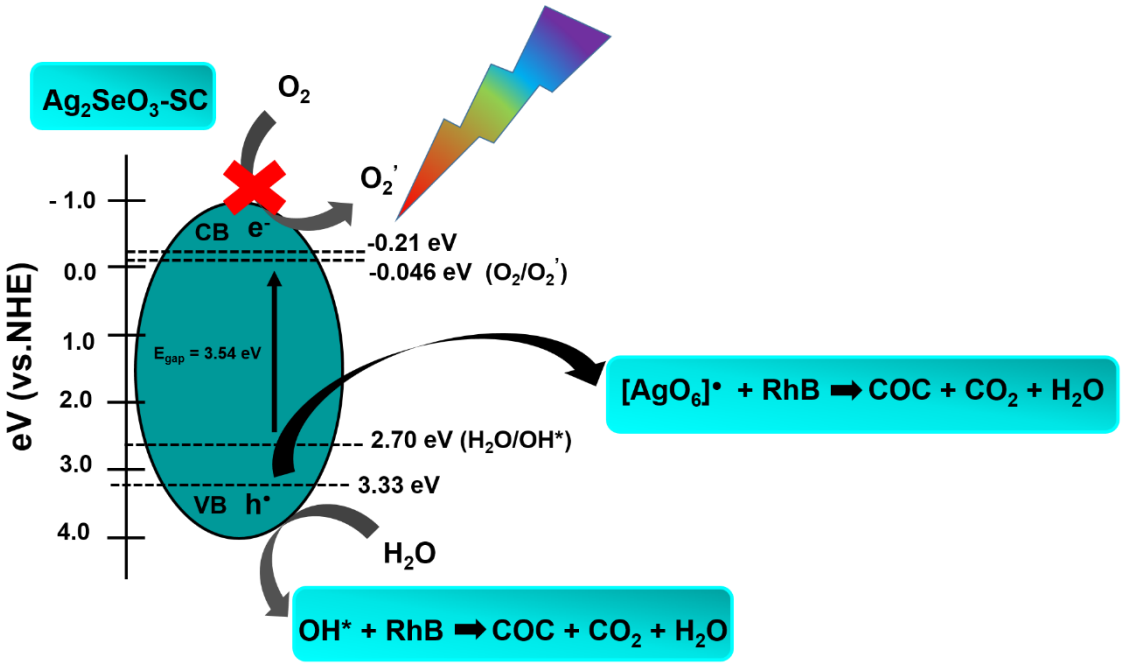

Fig. 21. Proposed photocatalytic mechanism for the Ag_2SeO_3-SC sample.

Conclusions

In summary, Ag_2SeO_3 monoclinic structure with different morphology has been successfully obtained by four synthesis methods, for the first time. Thermal analysis confirmed the phase stability up to 535 °C. XRD results confirmed the crystallinity of the samples without secondary phases, attesting long-range order of all samples. XPS analysis confirmed that the materials were pure and presented Se^{4+} species in all samples. Raman and FTIR spectroscopies attested the vibrational modes related to Se-O and Ag-O bonds indicating short-range structural order. FE-SEM images showed rods-, cube-, and faceted-like morphologies due to different methods of synthesis. UV-vis DRS and PL emissions are connected with results of photocatalytic activity, which attested Ag_2SeO_3-SC as the best performance photocatalyst and Ag_2SeO_3-CP as the higher PL intensity emission. Based on scavenger trapping experiments, the holes and hydroxyl radical, in minor extent, are the main reactive species during the photodegradation process, and a possible photocatalytic mechanism is proposed. The experimental and theoretical results, supported by first-principles calculations, at the DFT level, were analyzed in terms of the structural and electronic order/disorder effects. The relative stability of the eigth low-index surfaces of Ag_2SeO_3 were calculated to rationalize the crystal morphologies observed in FE-SEM images (using the Wulff construction) and different energy profiles associated with the transformation processes among morphologies were determined. Present results confirm the Ag_2SeO_3 based materials are promising photocatalyst with enhanced optical properties.

Conflicts of interest

There are no conflicts of interest to declare

Acknowledgments

The authors thank the support of the Brazilian research financing institution FAPESP (grant no. 2013/07296-2, grant no. 2019/03722-3, and grant no. 2019/25944-8). J.A. acknowledges Universitat Jaume I (project UJI-B2019-30), and the Ministerio de Ciencia, Innovación y Universidades (Spain) (project PGC2018094417-B-I00) for financially supporting this research. The authors also wish to thank Prof. Dr. Valmor Roberto Mastelaro (IFSC-USP), Rorivaldo Camargo (CDMF-UFSCar) and Sandra Maria Terenzi Bellini (CDMF-UFSCar) for technical and scientific contributions.

Supporting Information

The electronic supplementary information contain: Rietveld refinement plot; Atomic positions; Crystallographic data of Rietveld refinement; XPS core level spectra of Ag 3d, Se 3d, and O 1s; XPS elements positions and concentration; Band gap energy estimated by Kubelka and Munk; Surface area composition, E_{surf} and E_{poly} for the different proposed morphologies; and XRD patterns of the Ag_2SeO_3-SC catalysts after 3 photocatalytic cycles.

References

(1) Wu, V. M.; Ahmed, M. K.; Mostafa, M. S.; Uskoković, V. Empirical and Theoretical Insights into the Structural Effects of Selenite Doping in Hydroxyapatite and the Ensuing Inhibition of Osteoclasts. *Sci. Total Environ.* **2020**, *117*, 111257. https://doi.org/10.1016/j.scitotenv.2019.135577.

(2) Wang, X. X.; Li, X. B.; Hu, C. L.; Kong, F.; Mao, J. G. Ag4Hg(SeO3)2(SeO4): A Novel SHG Material Created in Mixed Valent Selenium Oxides by in Situ Synthesis. *Sci. China Mater.* **2019**, *62* (12), 1821–1830. https://doi.org/10.1007/s40843-019-1193-x.

(3) Qian, Q.; Kong, F.; Mao, J. G. A Series of New Silver Selenites with D0-TM Cations. *RSC Adv.* **2016**, *6* (83), 79681–79687. https://doi.org/10.1039/c6ra17867g.

(4) Shang, M.; Halasyamani, P. S. Mixed-Valent Selenium Compounds: Noncentrosymmetric Cd3(SeO3)2(SeO4) and Hg3(SeO3)2(SeO4) and Centrosymmetric Pb2(SeO3) (SeO4). *J. Solid State Chem.* **2020**, *286* (March), 2–7. https://doi.org/10.1016/j.jssc.2020.121292.

(5) Ma, Y. X.; Gong, Y. P.; Hu, C. L.; Kong, F.; Mao, J. G. BiGa(SeO3)3: A Phase Matchable SHG Material Achieved by Cation Substitution. *Inorg. Chem.* **2020**, *59* (11), 7852–7859. https://doi.org/10.1021/acs.inorgchem.0c00984.

(6) Steinhauser, G.; Luef, C.; Wildner, M.; Giester, G. Syntheses and Crystal Structures of Pb(SeO3)2 and Two Modifications of Sn(SeO3)2. *J. Alloys Compd.* **2006**, *419* (1–2), 45–49. https://doi.org/10.1016/j.jallcom.2005.10.003.

(7) Wildner, M.; Giester, G. Crystal Structures of SrSeO3 and CaSeO3 and Their Respective Relationships with Molybdomenite- and Monazite-Type Compounds - An Example for Stereochemical Equivalence of ESeO3 Groups (E = Lone Electron Pair) with Tetrahedral TO4 Groups. *Neues Jahrb. fur Mineral. Abhandlungen* **2007**,

184 (1), 29–37. https://doi.org/10.1127/0077-7757/2007/0083.

(8) Wu, C.; Jiang, X.; Lin, L.; Lin, Z.; Huang, Z.; Humphrey, M. G.; Zhang, C. AGa3F6(SeO3)2 (A = Rb, Cs): A New Type of Phase-Matchable Hexagonal Tungsten Oxide Material with Strong Second-Harmonic Generation Responses. *Chem. Mater.* **2020**, *32* (16), 6906–6915. https://doi.org/10.1021/acs.chemmater.0c01971.

(9) Giester, G.; Wildner, M. Hydrothermal Synthesis and Crystal Structure of Mn(SeO3)2. *J. Solid State Chem.* **1991**, *91*, 370–374.

(10) Bensch, W.; Gunter, J. R. The Crystal Structure of B-Zinc Selenite. **1986**, *174*, 291–295.

(11) Kohn, K.; Inoue, K.; Horie, O.; Akimoto, S. I. Crystal Chemistry of MSeO 3 and MTeO 3 (M = Mg, Mn, Co, Ni, Cu, and Zn). *J. Solid State Chem.* **1976**, *18* (1), 27–37. https://doi.org/10.1016/0022-4596(76)90075-X.

(12) Rademacher, O.; Göbel, H.; Oppermann, H. Crystal Structure of Bismuth Selenite, Bi2(SeO3)3. *Zeitschrift fur Krist. - New Cryst. Struct.* **2000**, *215* (3), 339–340. https://doi.org/10.1515/ncrs-2000-0316.

(13) Shi, L.; Mei, D.; Xu, J.; Wu, Y. Bi 2 O(XO 4)(IO 3) 2 (X = S, Se, Cr): Three-Dimensional Frameworks Containing [Bi 4 O 2] 8+ Clusters. *Solid State Sci.* **2016**, *63*, 54–61. https://doi.org/10.1016/j.solidstatesciences.2016.11.010.

(14) Jee Yoon Chung, Hongil Jo, Seongbeom Yeon, Hye Ryung Byun, Tae-Soo You, Joon I. Jang, and K. M. O. Bi3(SeO3)3(Se2O5)F: A Polar Bismuth Selenite Fluoride with Polyhedra of Highly Distortive Lone Pair Cations and Strong Second-Harmonic Generation Response. *Chem. Mater.* **2020**, *32* (17), 7318–7326. https://doi.org/10.1002/chin.201210016.

(15) Lee, D. W.; Oh, S. J.; Halasyamani, P. S.; Ok, K. M. New Quaternary Tellurite and Selenite: Synthesis, Structure, and Characterization of Centrosymmetric InVTe2O8 and Noncentrosymmetric InVSe2O8. *Inorg. Chem.* **2011**, *50* (10), 4473–4480. https://doi.org/10.1021/ic200135k.

(16) Gospodinov, G. G.; Stancheva, M. G. A Physicochemical Study of the Selenites of Yttrium. *J. Chem. Inf. Model.* **2019**, *53* (9), 1689–1699. https://doi.org/10.1017/CBO9781107415324.004.

(17) Bang, S. E.; Lee, D. W.; Ok, K. M. Variable Framework Structures and Centricities

in Alkali Metal Yttrium Selenites, AY(SeO3)2 (A = Na, K, Rb, and Cs). *Inorg. Chem.* **2014**, *53* (9), 4756–4762. https://doi.org/10.1021/ic500548v.

(18) Tuxworth, A. J.; Wang, C. H.; Evans, J. S. O. Synthesis, Characterisation and Properties of Rare Earth Oxyselenides A4O4Se3 (A = Eu, Gd, Tb, Dy, Ho, Er, Yb and Y). *Dalt. Trans.* **2015**, *44* (7), 3009–3019. https://doi.org/10.1039/c4dt03336a.

(19) Gu, J.; Zhao, Z. Q.; Ding, Y.; Chen, H. L.; Zhang, Y. W.; Yan, C. H. Liquid-Phase Syntheses and Material Properties of Two-Dimensional Nanocrystals of Rare Earth-Selenium Compound Containing Planar Se Layers: RESe2 Nanosheets and RE4O4Se3 Nanoplates. *J. Am. Chem. Soc.* **2013**, *135* (22), 8363–8371. https://doi.org/10.1021/ja4028583.

(20) Ionashiro, M.; Melios, C. B.; Ribeiro, C. A.; Crepsi, M. S.; Giolito, I. Thermal Decomposition of Hydrated Selenites of Trivalent Lanthanides and Yttrium. *Thermochimica Acta*. 1990, pp 223–232. https://doi.org/10.1016/0040-6031(90)80641-B.

(21) Pedro, M. de; Trombe, J. C.; Castro, A. On the Rare-Earth Selenites Pr2Se4011, R2Se309 and R2SeOs. *J. Mater. Sci. Lett.* **1995**, *14*, 994–997.

(22) Macedo, N. G.; Machado, T. R.; Roca, R. A.; Assis, M.; Foggi, C. C.; Puerto-Belda, V.; Mínguez-Vega, G.; Rodrigues, A.; San-Miguel, M. A.; Cordoncillo, E.; Beltrán-Mir, H.; Andrés, J.; Longo, E. Tailoring the Bactericidal Activity of Ag Nanoparticles/α-Ag 2 WO 4 Composite Induced by Electron Beam and Femtosecond Laser Irradiation: Integration of Experiment and Computational Modeling . *ACS Appl. Bio Mater.* **2019**, *2* (2), 824–837. https://doi.org/10.1021/acsabm.8b00673.

(23) Doster, J.; Baraldi, G.; Gonzalo, J.; Solis, J.; Hernandez-Rueda, J.; Siegel, J. Tailoring the Surface Plasmon Resonance of Embedded Silver Nanoparticles by Combining Nano- and Femtosecond Laser Pulses. *Appl. Phys. Lett.* **2014**, *104*, 153106. https://doi.org/10.1063/1.4871507.

(24) Lemire, J. A.; Harrison, J. J.; Turner, R. J. Antimicrobial Activity of Metals: Mechanisms, Molecular Targets and Applications. *Nat. Rev. Microbiol.* **2013**, *11* (6), 371–384. https://doi.org/10.1038/nrmicro3028.

(25) Longo, V. M.; De Foggi, C. C.; Ferrer, M. M.; Gouveia, A. F.; André, R. S.; Avansi, W.; Vergani, C. E.; Machado, A. L.; Andrés, J.; Cavalcante, L. S.; Hernandes, A. C.;

Longo, E. Potentiated Electron Transference in α-Ag2WO4 Microcrystals with Ag Nanofilaments as Microbial Agent. *J. Phys. Chem. A* **2014**, *118* (31), 5769–5778. https://doi.org/10.1021/jp410564p.

(26) De Foggi, C. C.; De Oliveira, R. C.; Fabbro, M. T.; Vergani, C. E.; Andres, J.; Longo, E.; Machado, A. L. Tuning the Morphological, Optical, and Antimicrobial Properties of α-Ag2WO4 Microcrystals Using Different Solvents. *Cryst. Growth Des.* **2017**, *17* (12), 6239–6246. https://doi.org/10.1021/acs.cgd.7b00786.

(27) Foggi, C. C.; Fabbro, M. T.; Santos, L. P. S.; de Santana, Y. V. B.; Vergani, C. E.; Machado, A. L.; Cordoncillo, E.; Andrés, J.; Longo, E. Synthesis and Evaluation of A-Ag2WO4 as Novel Antifungal Agent. *Chem. Phys. Lett.* **2017**, *674*, 125–129. https://doi.org/10.1016/j.cplett.2017.02.067.

(28) Machado, T. R.; Macedo, N. G.; Assis, M.; Doñate-Buendia, C.; Mínguez-Vega, G.; Teixeira, M. M.; Foggi, C. C.; Vergani, C. E.; Beltrán-Mir, H.; Andrés, J.; Cordoncillo, E.; Longo, E. From Complex Inorganic Oxides to Ag-Bi Nanoalloy: Synthesis by Femtosecond Laser Irradiation. *ACS Omega* **2018**, *3* (8), 9880–9887. https://doi.org/10.1021/acsomega.8b01264.

(29) Pinatti, I. M.; Nogueira, I. C.; Pereira, W. S.; Pereira, P. F. S.; Gonçalves, R. F.; Varela, J. A.; Longo, E.; Rosa, I. L. V. Structural and Photoluminescence Properties of Eu3+ Doped α-Ag2WO4 Synthesized by the Green Coprecipitation Methodology. *Dalt. Trans.* **2015**, *44* (40), 17673–17685. https://doi.org/10.1039/c5dt01997d.

(30) Pinatti, I. M.; Ireland, T. G.; Fern, G. R.; Rosa, I. L. V.; Silver, J. Low Temperature Micro Raman and Laser Induced Upconversion and Downconversion Spectra of Europium Doped Silver Tungstate Ag2−3xEuxWO4 Nanorods. *J. Mater. Sci. Mater. Electron.* **2017**, *28* (10), 7029–7035. https://doi.org/10.1007/s10854-016-6077-x.

(31) Pinatti, I. M.; Fern, G. R.; Longo, E.; Ireland, T. G.; Pereira, P. F. S.; Rosa, I. L. V.; Silver, J. Luminescence Properties of α-Ag<inf>2</Inf>WO<inf>4</Inf> Nanorods Co-Doped with Li^{+} and Eu^{3+} Cations and Their Effects on Its Structure. *J. Lumin.* **2019**, *206*. https://doi.org/10.1016/j.jlumin.2018.10.104.

(32) Pinatti, I. M.; Pereira, P. F. S.; de Assis, M.; Longo, E.; Rosa, I. L. V. Rare Earth Doped Silver Tungstate for Photoluminescent Applications. *J. Alloys Compd.* **2019**, *771*, 433–447. https://doi.org/10.1016/j.jallcom.2018.08.302.

(33) Fabbro, M. T.; Foggi, C. C.; Santos, L. P. S.; Gracia, L.; Perrin, A.; Perrin, C.; Vergani, C. E.; Machado, A. L.; Andrés, J.; Cordoncillo, E.; Longo, E. Synthesis, Antifungal Evaluation and Optical Properties of Silver Molybdate Microcrystals in Different Solvents: A Combined Experimental and Theoretical Study. *Dalt. Trans.* **2016**, *45* (26), 10736–10743. https://doi.org/10.1039/c6dt00343e.

(34) Oliveira, C. A.; Volanti, D. P.; Nogueira, A. E.; Zamperini, C. A.; Vergani, C. E.; Longo, E. Well-Designed β-Ag 2 MoO 4 Crystals with Photocatalytic and Antibacterial Activity. *Mater. Des.* **2017**, *115*, 73–81. https://doi.org/10.1016/j.matdes.2016.11.032.

(35) Silva, G. S.; Gracia, L.; Fabbro, M. T.; Serejo Dos Santos, L. P.; Beltrán-Mir, H.; Cordoncillo, E.; Longo, E.; Andrés, J. Theoretical and Experimental Insight on Ag2CrO4 Microcrystals: Synthesis, Characterization, and Photoluminescence Properties. *Inorg. Chem.* **2016**, *55* (17), 8961–8970. https://doi.org/10.1021/acs.inorgchem.6b01452.

(36) Fabbro, M. T.; Gracia, L.; Silva, G. S.; Santos, L. P. S.; Andrés, J.; Cordoncillo, E.; Longo, E. Understanding the Formation and Growth of Ag Nanoparticles on Silver Chromate Induced by Electron Irradiation in Electron Microscope: A Combined Experimental and Theoretical Study. *J. Solid State Chem.* **2016**, *239*, 220–227. https://doi.org/10.1016/j.jssc.2016.03.050.

(37) P. S., L.; G. S., S.; R. A., R.; M., A.; R., T.-M.; H., B.-M.; G., M.-V.; E., C.; J., A.; E., L. Laser and Electron Beam-Induced Formation of Ag/Cr Structures on Ag 2 CrO 4. *Phys. Chem. Chem. Phys.* **2019**, *21* (11), 6101–6111. https://doi.org/10.1039/c8cp07263a.

(38) Pinatti, I. M.; Tello, A. C. M.; Trench, A. B.; de Foggi, C. C.; Pereira, P. F. S.; Teixeira, M. M.; Jacomaci, N.; Andrés, J.; Longo, E. Zinc-Substituted Ag2CrO4: A Material with Enhanced Photocatalytic and Biological Activity. *J. Alloys Compd.* **2020**, *835*, 1–17. https://doi.org/10.1016/j.jallcom.2020.155315.

(39) De Oliveira, R. C.; De Foggi, C. C.; Teixeira, M. M.; Da Silva, M. D. P.; Assis, M.; Francisco, E. M.; Pimentel, B. N. A. D. S.; Pereira, P. F. D. S.; Vergani, C. E.; Machado, A. L.; Andres, J.; Gracia, L.; Longo, E. Mechanism of Antibacterial Activity via Morphology Change of α-AgVO 3 : Theoretical and Experimental Insights. *ACS Appl. Mater. Interfaces* **2017**, *9* (13), 11472–11481.

https://doi.org/10.1021/acsami.7b00920.

(40) De Oliveira, R. C.; Assis, M.; Teixeira, M. M.; Da Silva, M. D. P.; Li, M. S.; Andres, J.; Gracia, L.; Longo, E. An Experimental and Computational Study of β-AgVO3: Optical Properties and Formation of Ag Nanoparticles. *J. Phys. Chem. C* **2016**, *120* (22), 12254–12264. https://doi.org/10.1021/acs.jpcc.6b02840.

(41) Pimentel, B. N. A. da S.; de Foggi, C. C.; Barbugli, P. A.; de Oliveira, R. C.; de Avila, E. D.; Longo, E.; Vergani, C. E. Antifungal Activity and Biocompatibility of α-AgVO3 Microcrystals: A Promising Material against Oral Candida Disease. *Mater. Sci. Eng. C* **2020**, *108*, 110405. https://doi.org/10.1016/j.msec.2019.110405.

(42) Oliveira, R. C.; Teixeira, M. M.; Costa, J. P. C.; Penha, M.; Francisco, E. M.; da Silva, J. S.; Li, M. S.; Longo, E.; Gracia, L.; Andrés, J. α- and β-AgVO3 Polymorphs as Photoluminescent Materials: An Example of Temperature-Driven Synthesis. *Ceram. Int.* **2018**, *44* (6), 5939–5944. https://doi.org/10.1016/j.ceramint.2017.12.161.

(43) De Oliveira, R. C.; Gracia, L.; Assis, M.; Li, M. S.; Andres, J.; Longo, E.; Cavalcante, L. S. Disclosing the Electronic Structure and Optical Properties of Ag4V2O7 Crystals: Experimental and Theoretical Insights. *CrystEngComm* **2016**, *18* (34), 6483–6491. https://doi.org/10.1039/c6ce01269h.

(44) de Oliveira, R. C.; Zanetti, S. M.; Assis, M.; Penha, M.; Mondego, M.; Cilense, M.; Longo, E.; Cavalcante, L. S. Effect of Metallic Ag Growth on the Electrical Resistance of 3D Flower-like Ag4V2O7 Crystals. *J. Am. Ceram. Soc.* **2017**, *100* (6), 2358–2362. https://doi.org/10.1111/jace.14803.

(45) dos Santos, C. C.; Assis, M.; Machado, T. R.; dos Santos Pereira, P. F.; Minguez-Vega, G.; Cordoncillo, E.; Beltran-Mir, H.; Doñate-Buendía, C.; Andrés, J.; Longo, E. Proof-of-Concept Studies Directed toward the Formation of Metallic Ag Nanostructures from Ag 3 PO 4 Induced by Electron Beam and Femtosecond Laser. *Part. Part. Syst. Charact.* **2019**, *1800533*, 1–9. https://doi.org/10.1002/ppsc.201800533.

(46) Botelho, G.; Andres, J.; Gracia, L.; Matos, L. S.; Longo, E. Photoluminescence and Photocatalytic Properties of Ag3PO4Microcrystals: An Experimental and Theoretical Investigation. *Chempluschem* **2016**, *81* (2), 202–212. https://doi.org/10.1002/cplu.201500485.

(47) Botelho, G.; Sczancoski, J. C.; Andres, J.; Gracia, L.; Longo, E. Experimental and Theoretical Study on the Structure, Optical Properties, and Growth of Metallic Silver Nanostructures in Ag 3 PO 4. *J. Phys. Chem. C* **2015**, *119* (11), 6293–6306. https://doi.org/10.1021/jp512111v.

(48) Shen, J.; Lu, Y.; Liu, J. K.; Yang, X. H. Photocatalytic Activity of Silver Chromate Materials by Various Synthesis Methods. *J. Exp. Nanosci.* **2016**, *11* (8), 650–659. https://doi.org/10.1080/17458080.2015.1110624.

(49) Xu, D.; Cao, S.; Zhang, J.; Cheng, B.; Yu, J. Effects of the Preparation Method on the Structure and the Visible-Light Photocatalytic Activity of Ag2CrO4. *Beilstein J. Nanotechnol.* **2014**, *5* (1), 658–666. https://doi.org/10.3762/bjnano.5.77.

(50) Andrade Neto, N. F.; Silva, J. M. P.; Tranquilin, R. L.; Longo, E.; Bomio, M. R. D.; Motta, F. V. Stabilization of the γ-Ag2WO4 Metastable Pure Phase by Coprecipitation Method Using Polyvinylpyrrolidone as Surfactant: Photocatalytic Property. *Ceram. Int.* **2020**, *46* (10), 14864–14871. https://doi.org/10.1016/j.ceramint.2020.03.012.

(51) Macedo, N. G.; Gouveia, A. F.; Roca, R. A.; Assis, M.; Gracia, L.; Andrés, J.; Leite, E. R.; Longo, E. Surfactant-Mediated Morphology and Photocatalytic Activity of α-Ag2WO4 Material. *J. Phys. Chem. C* **2018**, *122* (15), 8667–8679. https://doi.org/10.1021/acs.jpcc.8b01898.

(52) Dovesi, R.; Erba, A.; Orlando, R.; Zicovich-Wilson, C. M.; Civalleri, B.; Maschio, L.; Rérat, M.; Casassa, S.; Baima, J.; Salustro, S.; Kirtman, B. Quantum-Mechanical Condensed Matter Simulations with CRYSTAL. *Wiley Interdiscip. Rev. Comput. Mol. Sci.* **2018**, *8* (4), 1–36. https://doi.org/10.1002/wcms.1360.

(53) Lee, C.; Hill, C.; Carolina, N. Development of the Colle-Salvetti Correlation-Energy Formula into a Functional of the Electron Density. *Chem. Phys. Lett.* **1989**, *162* (3), 165–169. https://doi.org/10.1016/0009-2614(89)85118-8.

(54) Peintinger, M. F.; Oliveira, D. V.; Bredow, T. Consistent Gaussian Basis Sets of Triple-Zeta Valence with Polarization Quality for Solid-State Calculations. *J. Comput. Chem.* **2013**, *34* (6), 451–459. https://doi.org/10.1002/jcc.23153.

(55) Doll, K.; Pyykkö, P.; Stoll, H. Closed-Shell Interaction in Silver and Gold Chlorides. *J. Chem. Phys.* **1998**, *109* (6), 2339–2345. https://doi.org/10.1063/1.476801.

(56) Pack, J. D.; Monkhorst, H. J. “special Points for Brillouin-Zone Integrations”-a

Reply. *Phys. Rev. B* **1977**, *16* (4), 1748–1749. https://doi.org/10.1103/PhysRevB.16.1748.

(57) Barmparis, G. D.; Lodziana, Z.; Lopez, N.; Remediakis, I. N. Nanoparticle Shapes by Using Wulff Constructions and First-Principles Calculations. *Beilstein J. Nanotechnol.* **2015**, *6* (1), 361–368. https://doi.org/10.3762/bjnano.6.35.

(58) Yan, S.; Wu, G. Application of Random Walk Model to Fit Temperature in 46 Gamma World Cities from 1901 to 1998. *Nat. Sci.* **2010**, *02* (12), 1425–1431. https://doi.org/10.4236/ns.2010.212174.

(59) Ferrer, M. M.; Gouveia, A. F.; Gracia, L.; Longo, E.; Andrés, J. A 3D Platform for the Morphology Modulation of Materials: First Principles Calculations on the Thermodynamic Stability and Surface Structure of Metal Oxides: Co3O4, α-Fe2O3, and In2O3. *Model. Simul. Mater. Sci. Eng.* **2016**, *24*, 025007. https://doi.org/10.1088/0965-0393/24/2/025007.

(60) Okkonen, P.; Hiltunen, L.; Koskenlinna, M.; Niinisto, L. Crystal Structure and Termal Stability of Silver Selenite. *Acta Chem. Scand.* **1994**, *48*, 857–860.

(61) Dutton, W. A.; Steen, A. J.; Themelis, N. J. Recovery of Selenium from Copper Anode Slimes. *Metall. Mater. Trans. B* **2008**, *2* (11), 3091–3097. https://doi.org/10.1007/bf02814960.

(62) Taskinen, P.; Patana, S.; Kobylin, P.; Latostenmaa, P. Oxidation Mechanism of Silver Selenide. *Oxid. Met.* **2014**, *81* (5–6), 503–513. https://doi.org/10.1007/s11085-013-9461-4.

(63) Assal, J.; Hallstedt, B.; Gauckler, L. J. Thermodynamic Assessment of the Silver–Oxygen System. *J. Am. Ceram. Soc.* **1997**, *80* (12), 3054–3460. https://doi.org/10.1016/0364-5916(92)90038-Y.

(64) Finger, L. W.; Cox, D. E.; Jephcoat, A. P. Correction for Powder Diffraction Peak Asymmetry Due to Axial Divergence. *J. Appl. Crystallogr.* **1994**, *27* (pt 6), 892–900. https://doi.org/10.1107/S0021889894004218.

(65) Stephens, P. W. Phenomenological Model of Anisotropic Peak Broadening in Powder Diffraction. *J. Appl. Crystallogr.* **1999**, *32* (2), 281–289. https://doi.org/10.1107/S0021889898006001.

(66) Toby, B. H. General Structure Analysis System - GSAS / EXPGUI, A Graphical User Interface for GSAS. *J. Appl. Crystallogr.* **2001**, *34* (1994), 210–213.

https://doi.org/10.1007/s10701-007-9105-0.

(67) Momma, K.; Izumi, F. VESTA 3 for Three-Dimensional Visualization of Crystal, Volumetric and Morphology Data. *J. Appl. Crystallogr.* **2011**, *44* (6), 1272–1276. https://doi.org/10.1107/S0021889811038970.

(68) Momma, K.; Izumi, F. VESTA : A Three-Dimensional Visualization System for Electronic and Structural Analysis . *J. Appl. Crystallogr.* **2008**, *41* (3), 653–658. https://doi.org/10.1107/s0021889808012016.

(69) Zhu, J.; Fan, H.; Sun, J.; Ai, S. Anion-Exchange Precipitation Synthesis of α-Ag2WO 4/Zn-Cr Layered Double Hydroxides Composite with Enhanced Visible-Light-Driven Photocatalytic Activity. *Sep. Purif. Technol.* **2013**, *120*, 134–140. https://doi.org/10.1016/j.seppur.2013.09.043.

(70) Lin, Z.; Li, J.; Zheng, Z.; Yan, J.; Liu, P.; Wang, C.; Yang, G. Electronic Reconstruction of α-Ag $_2$ WO $_4$ Nanorods for Visible-Light Photocatalysis. *ACS Nano* **2015**, *9* (7), 7256–7265. https://doi.org/10.1021/acsnano.5b02077.

(71) Wang, Z.; Sun, Q.; Wang, D.; Hong, Z.; Qu, Z.; Li, X. Hollow ZSM-5 Zeolite Encapsulated Ag Nanoparticles for SO2-Resistant Selective Catalytic Oxidation of Ammonia to Nitrogen. *Sep. Purif. Technol.* **2019**, *209* (July 2018), 1016–1026. https://doi.org/10.1016/j.seppur.2018.09.045.

(72) Zhou, M.; Wang, Z.; Sun, Q.; Wang, J.; Zhang, C.; Chen, D.; Li, X. High-Performance Ag-Cu Nanoalloy Catalyst for the Selective Catalytic Oxidation of Ammonia. *ACS Appl. Mater. Interfaces* **2019**, *11*, 46875–46885. https://doi.org/10.1021/acsami.9b16349.

(73) Zhang, X.; Yang, Y.; Song, L.; Wang, Y.; He, C.; Wang, Z.; Cui, L. High and Stable Catalytic Activity of Ag/Fe2O3 Catalysts Derived from MOFs for CO Oxidation. *Mol. Catal.* **2018**, *447* (January), 80–89. https://doi.org/10.1016/j.mcat.2018.01.007.

(74) Yuan, X.; Xue, S.; Liao, J.; Peng, F.; Shao, L.; Zhang, J. A Robust Approach to Fabricate CZTSSe Absorber Layer for Solar Cells via a Self-Selenizations Process Conducted by Concentrated Selenium Solution. *Mater. Res. Express* **2018**, *5*, 016413.

(75) Naveau, A.; Monteil-Rivera, F.; Guillon, E.; Dumonceau, J. Interactions of Aqueous Selenium (-II) and (IV) with Metallic Sulfide Surfaces. *Environ. Sci. Technol.* **2007**,

41 (15), 5376–5382. https://doi.org/10.1021/es0704481.

(76) Cui, X.; Yu, S. H.; Li, L.; Biao, L.; Li, H.; Mo, M.; Liu, X. M. Selective Synthesis and Characterization of Single-Crystal Silver Molybdate/Tungstate Nanowires by a Hydrothermal Process. *Chem. - A Eur. J.* **2004**, *10* (1), 218–223. https://doi.org/10.1002/chem.200305429.

(77) Huang, S.; Zhang, X.; Wang, L.; Bai, L.; Xu, J.; Li, C.; Yang, P. Controllable Synthesis and Tunable Luminescence Properties of Y 2(WO 4) 3:Ln 3+ (Ln = Eu, Yb/Er, Yb/Tm and Yb/Ho) 3D Hierarchical Architectures. *Dalt. Trans.* **2012**, *41* (18), 5634–5642. https://doi.org/10.1039/c2dt30221g.

(78) Andrés, J.; Gracia, L.; Gonzalez-Navarrete, P.; Longo, V. M.; Avansi, W.; Volanti, D. P.; Ferrer, M. M.; Lemos, P. S.; La Porta, F. A.; Hernandes, A. C.; Longo, E. Structural and Electronic Analysis of the Atomic Scale Nucleation of Ag on α-Ag2WO4 Induced by Electron Irradiation. *Sci. Rep.* **2014**, *4*, 1–7. https://doi.org/10.1038/srep05391.

(79) Zhang, X. Y.; Wang, J. D.; Liu, J. K.; Yang, X. H.; Lu, Y. Construction of Silver Tungstate Multilevel Sphere Clusters by Controlling the Energy Distribution on the Crystal Surface. *CrystEngComm* **2015**, *17* (5), 1129–1138. https://doi.org/10.1039/c4ce02089h.

(80) Tan, X.; Fan, Q.; Wang, X.; Grambow, B. Eu(III) Sorption to TiO2 (Anatase and Rutile): Batch, XPS, and EXAFS Studies. *Environ. Sci. Technol.* **2009**, *43* (9), 3115–3121. https://doi.org/10.1021/es803431c.

(81) Wang, B. Y.; Zhang, G. Y.; Cui, G. W.; Xu, Y. Y.; Liu, Y.; Xing, C. Y. Controllable Fabrication of α-Ag 2 WO 4 Nanorod-Clusters with Superior Simulated Sunlight Photocatalytic Performance. *Inorg. Chem. Front.* **2019**, *6* (1), 209–219. https://doi.org/10.1039/c8qi01025k.

(82) Catto, A. C.; Fiorido, T.; Souza, É. L. S.; Avansi, W.; Andres, J.; Aguir, K.; Longo, E.; Cavalcante, L. S.; da Silva, L. F. Improving the Ozone Gas-Sensing Properties of CuWO 4 Nanoparticles. *J. Alloys Compd.* **2018**, *748*, 411–417. https://doi.org/10.1016/j.jallcom.2018.03.104.

(83) Bachvarova, A.; Dimitriev, Y.; Iordanova, R. Glass Formation in the Systems Ag2SeO3-M NOm and CuSeO3-MnOm (MnOm = B2O3, MoO3). *J. Non. Cryst. Solids* **2005**, *351* (12–13), 998–1002.

https://doi.org/10.1016/j.jnoncrysol.2004.12.011.

(84) Kora, A. J.; Rastogi, L. Biomimetic Synthesis of Selenium Nanoparticles by Pseudomonas Aeruginosa ATCC 27853: An Approach for Conversion of Selenite. *J. Environ. Manage.* **2016**, *181*, 231–236. https://doi.org/10.1016/j.jenvman.2016.06.029.

(85) Ma, J.; Wang, Y.; Zhou, L.; Zhang, S. Preparation and Characterization of Selenite Substituted Hydroxyapatite. *Mater. Sci. Eng. C* **2013**, *33* (1), 440–445. https://doi.org/10.1016/j.msec.2012.09.011.

(86) Deb, B.; Ghosh, A. Synthesis and Characterization of AgI–Ag 2 O–SeO 2 Glass-Nanocomposites Embedded with β -AgI and Ag 2 SeO 3 Nanocrystals. *J. Nanosci. Nanotechnol.* **2010**, *10* (10), 6752–6759. https://doi.org/10.1166/jnn.2010.2640.

(87) Sathianandan, K.; McCory, L. D.; Margrave, J. L. Infrared Absorption Spectra of Inorganic Solids-III Selenates and Selenites. *Spectrochim. Acta* **1964**, *20* (6), 957–963. https://doi.org/10.1016/0371-1951(64)80096-5.

(88) Pereira, P. F. S.; Santos, C. C.; Gouveia, A. F.; Ferrer, M. M.; Pinatti, I. M.; Botelho, G.; Sambrano, J. R.; Rosa, I. L. V.; Andrés, J.; Longo, E. α-Ag2-2xZnxWO4 (0 ≤ × ≤ 0.25) Solid Solutions: Structure, Morphology, and Optical Properties. *Inorg. Chem.* **2017**, *56* (13), 7360–7372. https://doi.org/10.1021/acs.inorgchem.7b00201.

(89) Jun, G.; Liping, J.; Junjie, Z. Crystal Formation and Growth Mechanism of Inorganic Nanomaterials in Sonochemical Syntheses. *Sci. China Chem.* **2012**, *55* (11), 2292–2310. https://doi.org/10.1007/s11426-012-4732-5.

(90) Sushko, M. L. Understanding the Driving Forces for Crystal Growth by Oriented Attachment through Theory and Simulations. *J. Mater. Res.* **2019**, *34* (17), 2914–2927. https://doi.org/10.1557/jmr.2019.151.

(91) Li, D.; Nielsen, M. H.; Lee, J. R. I.; Frandsen, C.; Banfield, J. F.; De Yoreo, J. J. Direction-Specific Interactions Control Crystal Growth by Oriented Attachment. *Science (80-.).* **2012**, *336* (6084), 1014–1018. https://doi.org/10.1126/science.1219643.

(92) Kröger, F. A.; Vink, H. J. Relations between the Concentrations of Imperfections in Crystalline Solids. *Solid State Phys. - Adv. Res. Appl.* **1956**, *3* (C), 307–435. https://doi.org/10.1016/S0081-1947(08)60135-6.

(93) Wood, D. L.; Tauc, J. Weak Absorption Tails in Amorphous Semiconductors. *Phys.*

Rev. B **1972**, *5* (8), 3144–3151. https://doi.org/10.1103/PhysRevB.5.3144.

(94) Philips-Invernizzi, B. Bibliographical Review for Reflectance of Diffusing Media. *Opt. Eng.* **2002**, *40* (6), 1082. https://doi.org/10.1117/1.1370387.

(95) Longo, E.; Volanti, D. P.; Longo, V. M.; Gracia, L.; Nogueira, I. C.; Almeida, M. A. P.; Pinheiro, A. N.; Ferrer, M. M.; Cavalcante, L. S.; Andrés, J. Toward an Understanding of the Growth of Ag Filaments on α-Ag 2WO4 and Their Photoluminescent Properties: A Combined Experimental and Theoretical Study. *J. Phys. Chem. C* **2014**, *118* (2), 1229–1239. https://doi.org/10.1021/jp408167v.

(96) Oseghe, E. O.; Ofomaja, A. E. Facile Microwave Synthesis of Pine Cone Derived C-Doped TiO2 for the Photodegradation of Tetracycline Hydrochloride under Visible-LED Light. *J. Environ. Manage.* **2018**, *223* (July), 860–867. https://doi.org/10.1016/j.jenvman.2018.07.003.

(97) Yang, L.; Liu, B.; Liu, T.; Ma, X.; Li, H.; Yin, S.; Sato, T.; Wang, Y. A P25/(NH4)XWO3hybrid Photocatalyst with Broad Spectrum Photocatalytic Properties under UV, Visible, and near-Infrared Irradiation. *Sci. Rep.* **2017**, *8* (March), 1–11. https://doi.org/10.1038/srep45715.

(98) Li, S.; Cai, J.; Wu, X.; Zheng, F.; Lin, X.; Liang, W.; Chen, J.; Zheng, J.; Lai, Z.; Chen, T.; Zhu, L. Fabrication of Positively and Negatively Charged, Double-Shelled, Nanostructured Hollow Spheres for Photodegradation of Cationic and Anionic Aromatic Pollutants under Sunlight Irradiation. *Appl. Catal. B Environ.* **2014**, *160–161* (1), 279–285. https://doi.org/10.1016/j.apcatb.2014.05.021.

(99) Dai, G.; Yu, J.; Liu, G. A New Approach for Photocorrosion Inhibition of Ag 2CO 3 Photocatalyst with Highly Visible-Light-Responsive Reactivity. *J. Phys. Chem. C* **2012**, *116* (29), 15519–15524. https://doi.org/10.1021/jp305669f.

(100) Wang, W.; Cheng, B.; Yu, J.; Liu, G.; Fan, W. Visible-Light Photocatalytic Activity and Deactivation Mechanism of Ag 3PO 4 Spherical Particles. *Chem. - An Asian J.* **2012**, *7* (8), 1902–1908. https://doi.org/10.1002/asia.201200197.

(101) Ray, S. K.; Dhakal, D.; Lee, S. W. Rapid Degradation of Naproxen by AgBr-A-NiMoO4 Composite Photocatalyst in Visible Light: Mechanism and Pathways. *Chem. Eng. J.* **2018**, *347* (January), 836–848. https://doi.org/10.1016/j.cej.2018.04.165.

(102) Montoya, J. F.; Velásquez, J. A.; Salvador, P. The Direct-Indirect Kinetic Model in

Photocatalysis: A Reanalysis of Phenol and Formic Acid Degradation Rate Dependence on Photon Flow and Concentration in TiO2 Aqueous Dispersions. *Appl. Catal. B Environ.* **2009**, *88* (1–2), 50–58. https://doi.org/10.1016/j.apcatb.2008.09.035.

(103) Zhang, N.; Zhang, X.; Gan, C.; Zhang, J.; Liu, Y.; Zhou, M.; Zhang, C.; Fang, Y. Heterostructural Ag 3 PO 4 /UiO-66 Composite for Highly Efficient Visible-Light Photocatalysts with Long-Term Stability. *J. Photochem. Photobiol. A Chem.* **2019**, *376* (November 2018), 305–315. https://doi.org/10.1016/j.jphotochem.2019.03.025.

(104) Xu, H.; Cao, Y.; Xie, J.; Hu, J.; Li, Y.; Jia, D. A Construction of Ag-Modified Raspberry-like AgCl/Ag2WO4 with Excellent Visible-Light Photocatalytic Property and Stability. *Mater. Res. Bull.* **2018**, *102*, 342–352. https://doi.org/10.1016/j.materresbull.2018.02.047.

For Table of Contents Only

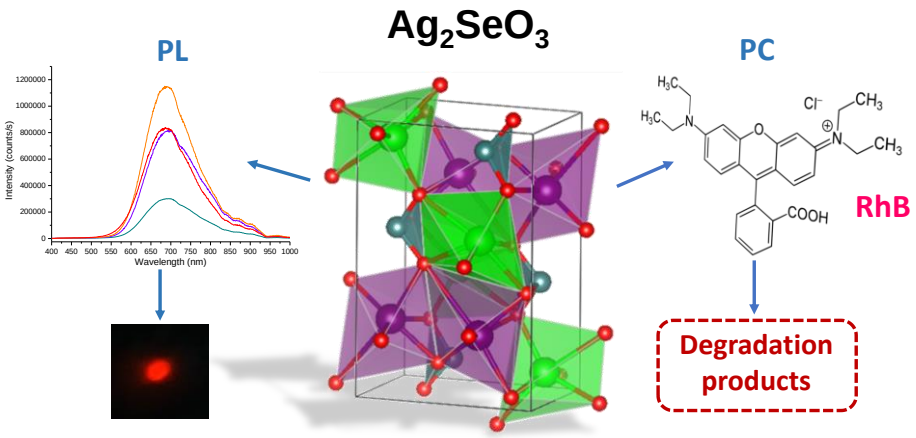

Synopsis: Silver selenite (Ag_2SeO_3) appears as a multifunctional material that can act both for photoluminescence (PL) or photocatalytic (PC) applications. Different synthesis methods employed allow modulation of its properties and morphologies. PL emission spectra present an intense band in the red region, which is useful for optical devices. PC analysis attest material´s efficacy in degradation of Rhodamine B, being an indicative for others catalysis routes. Finally, DFT calculation performed corroborate with the findings herein described.